hydrogen

MDPI

Article

From Flowability to Stress Transfer: Experimental Characterization of $TiFe_{(1-x)}Mn_x$ ($x \approx 0.1$) Intermetallic Powders for Solid-State Hydrogen Storage

Chrisale Ngueloheu Yeda [1], Thomas Jeannin [1], Aurélien Neveu [2], David Chapelle [1] and Anne Maynadier [1,*]

[1] Université Marie et Louis Pasteur, CNRS, FEMTO-ST Institute, FCLAB, F-25000 Besançon, France; chrisale.ngueloheu_yeda@umlp.fr (C.N.Y.) ; thomas.jeannin@umlp.fr (T.J.); david.chapelle@univ-fcomte.fr (D.C.)
[2] Granutools, 4340 Awans, Belgium; aurelien.neveu@granutools.com
* Correspondence: anne.maynadier@umlp.fr

Abstract

In a solid-state hydrogen storage tank, the storage medium is most often in the form of an intermetallic alloy powder. With each cycle of hydrogen absorption/desorption, the particles swell, move, fragment, and segregate. Understanding and modeling these phenomena are essential in order to guide engineers during the tank design process. However, there are little data in the literature on the mechanical behavior of powders for storage applications. This study focuses on the flowability and compression behavior of an intermetallic powder, with the aim of analyzing particle mobility in a confined environment as well as the transmission of forces to the tank walls. In order to represent the evolution of particle size through fragmentation during cycles, five $TiFe_{(1-x)}Mn_x$ ($x \approx 0.1$) powders, differing in their average particle size and polydispersity, are studied. Flowability tests on Granutools® (Awans, Belgium) instruments show that behaviors differ. Fine-grained samples exhibit rheo-thickening behavior, while coarser samples are quasi-Newtonian. These tests highlight variations in cohesion and internal friction, particularly for polydisperse samples. Stepwise cyclic compression tests (in stages 0-10-20-30 kN) were performed to study the elastic response of the powder under confinement and its ability to transfer stresses to the walls. This work highlights the impact of particle size and polydispersity on stress transfer in a confined space. This work therefore presents the mechanical effects of changes in particle size and polydispersity during absorption/desorption cycles on the overall behavior of the powder storage bed, in terms of flowability, cohesion, and stress transmission, in order to better understand, in the long term, its impact on tank deformation.

Keywords: intermetallic compound; powder mechanics; powder bed breathing; segregation; flowability; compressibility; solid-state hydrogen storage

Academic Editor: Zhang-Hui Lu

Received: 6 February 2026
Revised: 16 March 2026
Accepted: 20 March 2026
Published: 24 March 2026

1. Introduction

The relevance of hydrogen as an energy carrier and its role in the ecological transition toward decarbonization of industry are now well established [1,2]. Safe and energy-efficient storage solutions are essential to ensuring its green credentials. A sustainable hydrogen storage solution must enable the electrical reconversion of green hydrogen—

produced by water electrolysis using surplus electricity from renewable sources (wind, tidal, solar…)—at a period of peak demand [3].

A broad spectrum of technological pathways are currently being investigated for the storage and transportation of hydrogen. The most mature solutions are based on physical storage principles, namely compressed gaseous hydrogen (CGH) (typically 350 bar or 700 bar) [4], cryogenic storage in liquefied state (at −253 °C) [5], and hybrid cryo-compressed systems combining both approaches [6] operating within pressure ranges of approximately 200–300 bar and temperatures between −230 and −400 °C, depending on the specific technology. However, the three approaches are inherently constrained by the substantial energy required for gas compression or continuous refrigeration, which is necessary to mitigate boil-off losses and maintain thermodynamic stability. Other hydrogen storage strategies rely on chemical conversion routes, such as transformation into borazane (NH_3BH_3), ammonia (NH_3), or liquid organic hydrogen carriers (LOHCs) [7,8]. These conversions are particularly well suited for long-distance transport, such as maritime transport, for example. However, they require large-scale chemical processing infrastructure to release and purify hydrogen at the end of the value chain, which significantly impacts the overall system complexity, security, efficiency and capital expenditure. Another major area concerns the storage and transport of hydrogen using carrier materials [8]. Some carrier materials are adsorption-based systems operating though physisorption mechanisms at the material surface, such as carbon nanostructures [9] or metal–organic frameworks [10]. Although these materials exhibit high specific areas and promising gravimetric capacities (until 14% for NU-1501-Al), their practical implementation requires very low temperatures and/or elevated pressures (in the order of −200 °C and 70 bar), limiting their large-scale deployment. Finally, solid-state hydrogen storage in metal hydrides [11] represents a technologically mature and scalable approach. This category encompasses ionic hydrides such as MgH_2 and intermetallic hydrides (AB, AB2, BCC, AB5-type compounds), which are among the most readily implementable systems and yet commercialized. Investigated since the 1980s, these materials enable reversible hydrogen storage under thermodynamic conditions close to ambient temperature, with hydrogen absorption and desorption controlled solely by adjusting the temperature and pressure within the storage vessel [12,13]. They are currently experiencing renewed interest driven by recent advances in high-entropy alloys (HEAs) [14–17], where compositional tuning strategies are being explored to optimize storage capacity, thermodynamic reversibility, and cycling stability.

Solid-state hydrogen storage relies on the reversible hydriding of intermetallic alloys to store hydrogen atoms within the bulk of the material [18]. This provides intrinsically safe hydrogen storage without requiring heavy infrastructure and also offers high energy efficiency as hydrogen absorption and desorption occur under relatively mild operating conditions, typically at low pressures (0–50 bar, thus minimizing compression requirement and leakage risks) and near ambient temperature (approximately 10–80 °C). Under such conditions, the volumetric hydrogen storage capacity generally ranges from 100 to 150 g/L, corresponding to hydrogen-to-metal atomic ratios (H/M) of approximately 1 to 2. These values exceed those achieved by high-pressure compressed hydrogen storage (≈39 g/L at 700 bar) and even by liquid hydrogen storage (≈71 g/L at −253 °C). Intermetallic compounds capable of reversible hydriding have further demonstrated significant potential in gas separation and purification processes [19], as well as in high-efficiency hydrogen compression technologies [14,20]. However, scientific and technological barriers are delaying its large industrial-scale deployment. On the one hand, the weight of the storage medium itself, most often in the form of metal powder, limits solid-state storage to stationary or heavy-mobility applications (gravimetric capacity < 3 wt%). On the other hand, storage powder ages during the operating life.

https://doi.org/10.3390/hydrogen7020044

During successive cycles of use (filling/emptying), the particles of the storage medium swell during absorption and shrink during desorption. Particles undergo decrepitation, meaning they self-fracture, segregate, and settle at the bottom of the storage tank [21–23]. Several experimental studies on intermetallic hydrides rely on cylindrical reactors instrumented with strain gauges stuck on the outer walls to evaluate the stresses generated during hydrogen cycling [24–27]. Charlas et al. [23] conducted a notable investigation of the motion and potential thrust force of a Ti–Cr–V + Zr–Ni hydride powder bed during H_2 cycling. They developed a multi-instrumented experimental setup equipped with thermocouples and a movable piston positioned at the free surface of the bed. Their results revealed two coupled phenomena: a cyclic rearrangement of particles within the powder bed, characterized by a decrease followed by an increase in porosity during each cycle, and a progressive densification of the packing over successive cycles. Okumura et al. [24,25] proposed an original approach to identify the densification gradient along the height of a reactor subjected to hydrogen cycling. Their method consists of slicing the reactor after operation and analyzing the powder contained in each layer. By combining these measurements with strain gauge data, they demonstrated a clear correlation between the measured hoop stresses and the local packing fraction. Complementary studies have employed X-ray computed tomography to investigate the rearrangement, densification, and settlement of hydride powder beds inside reactors before and after cycling [22,26]. These observations show that fine particles produced by decrepitation progressively migrate toward the bottom of the reactor, leading to higher packing densities in the lower regions of the bed, where the largest wall deformations are typically observed. This reorganization and settling of increasingly fine particles in the lower part of the tank generates, cycle after cycle, increasing stresses on the walls, leading to plastic deformation of the enclosure and irreversible damage (as reported in [21,26]).

Understanding these phenomena is important in order to guide engineers toward better tank design. It is therefore necessary to study the mechanical behavior of the concerned intermetallic powders, in order to characterize their ability to move or to transmit stresses within the containment vessel. These characterizations will be useful for modeling and understanding behavior, as demonstrated by B. Charlas [23] for the TiCrV alloy. Experimental studies [21,23,24,26] have shown a decrease in particle size with the number of breathing cycles (absorption/desorption). This decrease alters the mechanical interactions at the level of contact between particles or with the walls. G. Stahlkopf et al. [27] have demonstrated on an AB2 hydride-forming alloy using synchrotron radiation microcomputed tomography that particle aging—directly linked to both the initial and evolving local particle size distribution as well as the packing density evolution inside the storage vessels—plays a predominant role in determining the radial expansion forces exerted on the tank walls. They enhanced that the initial particle size and packing of the storage medium is critical on the intensity of the transmitted stresses and of the tank deformation.

The present work investigates the mechanical effects of particle size evolution—representative of that induced by hydride particle decrepitation during cyclic absorption/desorption—on the overall behavior of the granular bed. The objective is to elucidate its influence on stress transmission, deformation and potential damage mechanisms affecting the storage reservoir. The objective of this study is to analyze the flowability of the material under different solicitations and on powders of varying grain size and polydispersity, as well as to study their mechanical behavior under compression in a rigid matrix. This study simulates decrepitation-induced particle size evolution by employing mechanically crushed, sieved and mixed powders with controlled size distributions. All experiments were performed in ambient air; therefore, changes in particle morphology, surface roughness, and surface chemistry specific to decrepitation are not captured. Despite this limitation, the strength of this study lies in the combined and cross-analysis of complementary

experimental techniques, allowing robust behavioral trends to be identified. The proposed engineering-based methodology provides a practical framework for qualifying future innovative intermetallic alloy powders intended for hydrogen storage, compression or gas purification applications where cyclic stability is critical.

Finally, this study identifies the main behavioral trends that must be accounted for in order to enable their implementation in predictive models, such as discrete element modeling, at the macroscopic scale of the powder bed. Such an approach ultimately aims to provide reliable insight for the design and dimensioning of solid-state storage tanks.

The following section presents the powder samples considered in this study, as well as the experimental devices and associated methodologies. The flowability of the powder (i.e., its ability to flow) is examined under three conditions: dynamic, quasi-static, and static, allowing for the development of indicators for classifying powders. In addition, the study of compression in a matrix (quasi-oedometric compression), carried out using instrumentation designed specifically for this purpose, provides insight into the elastic properties of the powder bed and the transfer of forces to the walls depending on the packing fraction. The results obtained are presented in Section 3 and analyzed in Section 4 in order to identify the influence of particle size and polydispersity on the measured mechanical properties and on the proposed cohesion and flowability indicators. Finally, their implication for the behavior of the storage tank is discussed.

2. Materials and Methods

Dynamic testing is based on a device called a "GranuDrum" A rotating drum is used to study the powder in motion. The dynamic angle of repose θ is measured, defined as the angle formed between the free surface of the powder bed and the horizontal plane. The cohesive index is also characterized according to the shape fluctuation of the free surface. Quasi-static densification behavior is studied using the "GranuPack" device , which is based on tapped density analysis to evaluate the packing properties of powders. Finally, static stress is studied using the "GranuHeap" device : a free pile of powder is formed on a horizontal surface and the static angle of repose is evaluated by measuring the angle of heap formed. The three instruments are supplied by Granutools (Awans, Belgium) [28]. However, before introducing these tests, the following section presents the study material and the various samples.

2.1. Material Selection and Preparation of Powder Samples

The material considered in this study is $TiFe_{(1-x)}Mn_x$ ($x \approx 0.1$), one of the most widely used intermetallic compounds for industrial hydrogen storage owing to its good storage properties (at 20 °C : $P_{abs} \simeq 5\ bar, P_{des} \simeq 2.5\ bar$ defined at mid plateau, when $P_{saturation} \simeq 30\ bar$ for a theoretical gravimetric storage capacity of 1.89 wt% [29]), but also due to its controlled cost, availability and recyclability [30–32]. The powders used here have been produced by MAHYTEC (Dole, France). The synthesis is made by induction melting of the pure constituent elements, followed by homogenization. The molten alloy is then cast into an ingot and cooled under argon atmosphere before being crushed using a jaw crusher to obtain a millimetric powder. At the end of the production process, an X-ray fluorescence (XRF) analysis is performed on a representative sampling to validate composition and homogeneity. The resulting powder is then stored under vacuum.

After mechanical crushing, the particles exhibit a coarse size distribution and a markedly angular, faceted morphology resulting from cleavage-dominated brittle fracture during crushing (see Figure 1a). Following repeated hydrogen absorption–desorption cycles up to saturation, the particles undergo significant degradation due to decrepitation. The particle size distribution shifts toward finer fractions (mean size ~150 μm after 16 cycles), and the overall morphology becomes more rounded (see Figure 1b). Nevertheless, the

particles retain certain sharp edges and flat facets characteristic of brittle fracture mechanisms. A major evolution lies in the development of multidirectional cracks throughout the particles, affecting both the largest and the most fragmented ones (see Figure 1c). This cracking initiates from the activation stage (first hydriding) and progresses with each subsequent cycle, leading to gradual fragmentation upon cycling. It is noteworthy that even if the decrepitation of FeTi-type compounds appears to be slower and more gradual than of $LaNi_5$, several studies have shown that $LaNi_5$ particles also stay facetted with sharp edges even after 80 cyclic hydriding/dehydriding tests (see Figure 4 in [33] and Figure 5 in [21]), while the mean equivalent particle volume decreases by approximately 50%, with the mean apparent diameter stabilizing at around 20 µm [21,33].

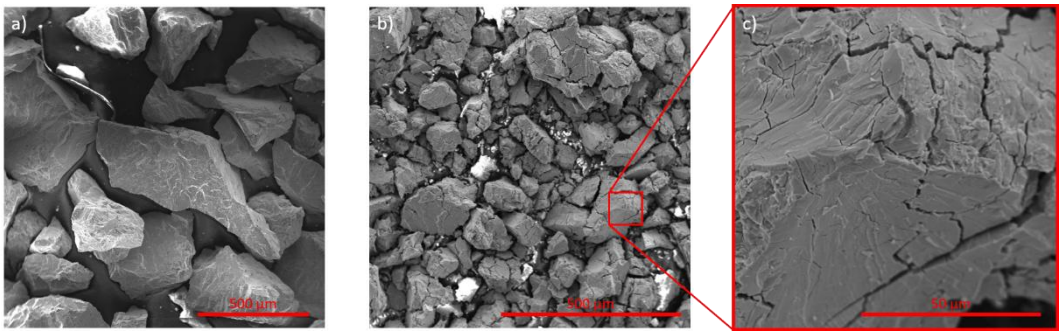

Figure 1. SEM micrographs of a $TiFe_{0.9}Mn_{0.1}$ powder: (**a**) raw crushed powder before any hydrogenation; (**b**) after 16 H_2 absorption/desorption cycles; (**c**) detail of one damaged particle. All images have been made on a JEOL JSM7800F SEM (Tokyo, Japan).

In order to simulate powders exhibiting various levels of granulometry and polydispersity induced by various stages of decrepitation, the original industrial powder is sieved into three powder batches with narrow and non-overlapping particle size intervals, making them quasi-monodisperse: P1 = [40 ; 200] µm; P2 = [300 ; 500] µm; P3 = [710 ; 1000] µm. Samples from P1 and P3 are then blended in equal masses to obtain the quasi-bidisperse powder P4. P1, P2 and P3 are also blended in equal masses to obtain the polydisperse powder P5. All preparation steps were therefore conducted under ambient air. It is acknowledged that such a methodology does not account for the modifications in particle morphology, surface roughness, or surface chemistry that inherently differ between decrepitation-driven fragmentation and mechanical crushing.

A granulometric analysis is then performed using a Laser Particle Size Analyzer (Partica Horiba model LA-960, Irvine, CA, USA). The particle size distributions are shown in Figure 2. For the three first powders, well-defined narrow modes were expected. It is confirmed for P2 and P3, but P1, the finest powder, does not present a strictly Gaussian statistical distribution; one can guess a second mode. Fortunately, P4 exhibits two distinct modes confirming bidispersity. P5 exhibits a broader, clearly polydisperse size distribution.

The quantitative data are summed up in Table 1, which indicates the volumetric percentiles and average diameters. Polydispersity is evaluated using the "span" indicator, which measures the relative width of the particle size distribution as $\frac{D_{90}-D_{10}}{D_{50}}$. If $span < 1$, the distribution is narrow and the powder can be considered quasi-monodisperse. $span \approx 1$ indicates a moderately polydisperse powder, while $span > 1.5$ indicates a wide and highly polydisperse distribution.

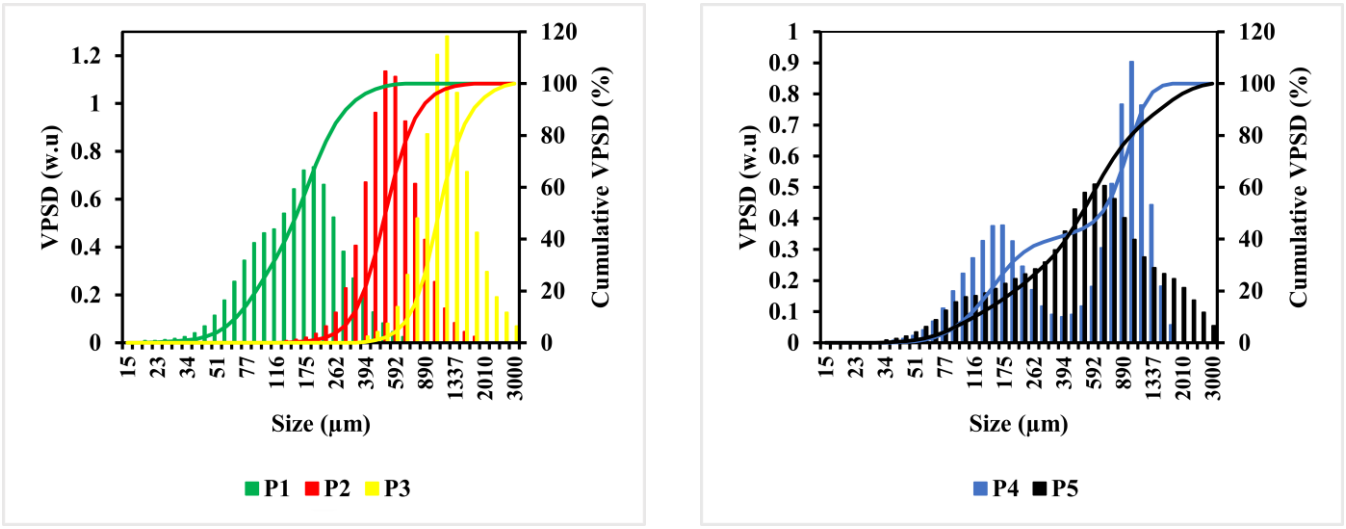

(**a**) (**b**)

Figure 2. Volume Particle Size Distribution (VPSD) of the five batches of (**a**) quasi-monodisperse powders P1, P2, P3 and (**b**) quasi-bidisperse powder P4, and polydisperse powder P5.

The samples have a wide range of median diameters, ranging from very fine (P1) to coarse (P3). P4 and P5 have intermediate median diameters. P4 and especially P5 are highly polydisperse, while P2 and P3 are relatively unimodal. Although P1 exhibits slight polydispersity and a minor secondary mode around 101 µm, the main mode dominates and its distribution overlaps very little with those of the other powders. For these reasons, P1 will be considered as quasi-monodisperse in the following discussion. The characterization of these samples will subsequently enable us to observe how particle size and mono-, bi- or polydisperse characteristics give rise to different mechanical behaviors, particularly with regard to flowability and stress transmission.

Table 1. Comparative granulometric analysis of quasi-monodisperses (P1, P2, P3) and mixed (P4, P5) powders. D_{10}, D_{50} and D_{90} stand for the diameters below which 10%, 50% or 90% respectively of the particle volume is found.

Powder	D10 (µm)	D50/Median (µm)	D90 (µm)	Span	Polydispersity
P1	67.77	154.66	300.68	1.53	High
P2	331.38	522.50	844.70	0.99	Moderate
P3	705.41	1074.92	1726.28	0.93	Moderate
P4	105.68	662.31	1156.55	1.57	High
P5	116.28	507.53	1469.05	2.64	Very High

2.2. Methods for Characterizing Flowability and Cohesion

The selection of experimental devices is motivated by the search for quantities that are easy to measure and depend on interactions between particles and their mechanical properties. We chose to use parameters such as the dynamic angle of repose θ [34] to evaluate the interactions between particles, as well as the elastic properties under compression of a confined powder bed to understand the elastic characteristics of the particles in the granular medium.

The "GranuDrum" device, shown in Figure 3, is used to characterize the flowability during the movement of the powder bed by measuring the dynamic angle of repose θ and the cohesive index CI [34]. It is a transparent rotating drum 84 mm in diameter and

20 mm wide, filled to 50% of its volume. It represents around 170 g for P1 and for P2, 164 g for P3, 200 g for P4 and for P5, with an uncertainty of 0.5 g.

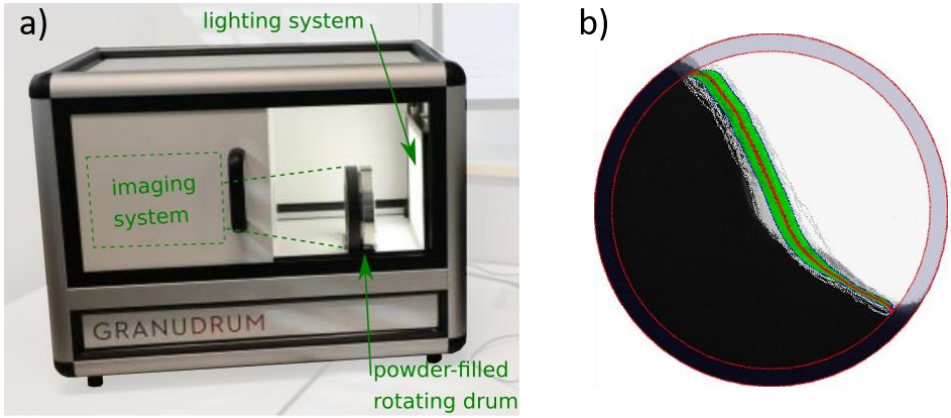

Figure 3. (**a**) GranuDrum device [34] incorporating a rotating drum, a lighting system, and an imaging system; (**b**) typical analysis image of the rotating drum containing an intermetallic powder (combination of 50 acquisitions): the average powder interface is highlighted in red and the envelope of fluctuations in green.

For each rotation speed (from 0 to 60 rpm), after stabilization, a camera acquires 50 images of the powder in the rotating drum. From the black and white images, an image analysis algorithm determines the coordinates of all points on the free surface of the powder, called the interface. The digital image processing is described in [34]. The dynamic angle of repose θ is evaluated using Equation (1) in a restricted diameter range at the center of the drum (see Figure 4a).

$$\theta = \tan^{-1}\left(\frac{y_{top}-y_{bottom}}{x_{top}-x_{bottom}}\right) \text{ (deg)} \quad (1)$$

The cohesion index CI is determined by evaluating the fluctuation of the powder interface in the drum, at a given speed, over the 50 images acquired (Figure 4b). CI is the average of the standard deviations $\sigma(x)$ of the interface vertical coordinates at each horizontal position, over a reduced area of interest D_{crop}. This diameter reduction prevents artifacts caused by particles stuck to the wall. The cohesion index CI is evaluated using Equation (2).

$$CI = \frac{1}{D_{crop}}\sum_x \sigma(x) \text{ (w.u)} \quad (2)$$

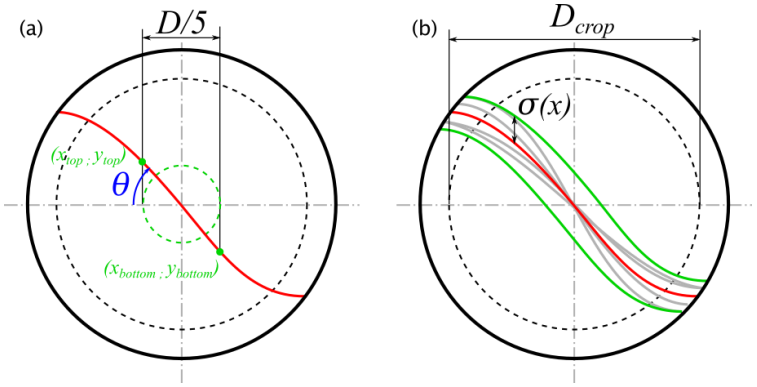

Figure 4. Schematic diagram of the rotating drum: (**a**) area of interest for the computation of the coordinates of the average powder interface (in red) and the dynamic angle of repose θ (in blue)

and (**b**) area of interest for computing the cohesion index, CI, via interface fluctuation (more details in [34]).

The second device, GranuPack (Figure 5), is used to evaluate the settling behavior of powders under quasi-static solicitations. The test procedure consists of pouring the powder in a cylindrical cell and then placing an aluminum disc on top to keep the upper surface flat. The device then performs "taps" by making repeated free falls of 1 mm in height at regular intervals. This procedure causes the powder to gradually settle, depending on the characteristics of the particles, such as their cohesion, friction, or morphology. After each tap, the powder height is measured by an inductive sensor, which allows the bulk density ρ of the powder to be calculated. This quantity allows indicators to be determined such as the Hausner ratio Hr (Equation (3)), the Carr Index C (Equation (4)), the characteristic tap number $n_{1/2}$ and the mobility index α [35]. The Hausner ratio Hr [36] and the Carr Index C [37] enable the flowability and cohesion of powders to be qualified. The Hausner ratio primarily reflects interparticle cohesion and internal friction, making it a useful indicator of flow resistance and sensitivity to arching under consolidation. In contrast, the Carr Index quantifies the compaction of the powder bed and is therefore more directly related to the ease with which interstitial voids are eliminated under tapping. The characteristic number $n_{1/2}$ (see Figure 5b) represents the number of "taps" required to achieve half of the maximum compaction, while the mobility index α, defined as the slope of the line tangent to the curve at the origin, provides information on the speed at which the powder settles under mechanical stress.

$$\mathrm{Hr} = \frac{\rho(n)}{\rho(0)} \ (\mathrm{w.u}) \tag{3}$$

With n the current number of taps

$$\mathrm{C} = 100\,\frac{\rho(n)-\rho(0)}{\rho(n)} \ (\mathrm{w.u}) \tag{4}$$

With $\rho(n)$ the bulk density of the powder at the end of « taps » n, $\rho(0)$ is the initial bulk density, before settling.

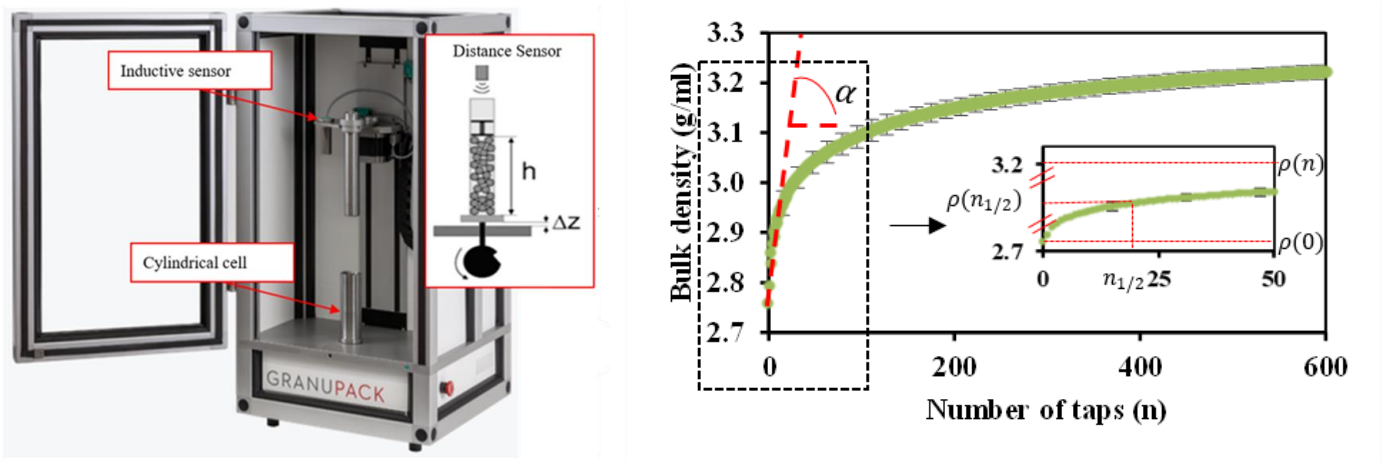

(**a**) (**b**)

Figure 5. (**a**) GranuPack device and its operating principle; (**b**) apparent bulk density ρ curve as a function of the number of falls n.

The third device, GranuHeap (Figure 6), allows the formation of a powder heap under the simple effect of gravity to be studied. A 40 mm internal diameter initialization tube, sliding on a rotating disc, is filled with the powder sample to be characterized. The tube then moves upward at a constant speed of 5 mm/s. The powder flows under the effect

of gravity and forms a stable heap on the disc-shaped support platform. Then, the support platform is rotated slowly (1 rpm) and a camera takes 16 snapshots over 180 degrees. The shape of the heap is treated by image analysis in order to determine the angle of static repose α_S as the average of the base angles of the 16 isosceles triangles with the same projected area [28] (Figure 6b).

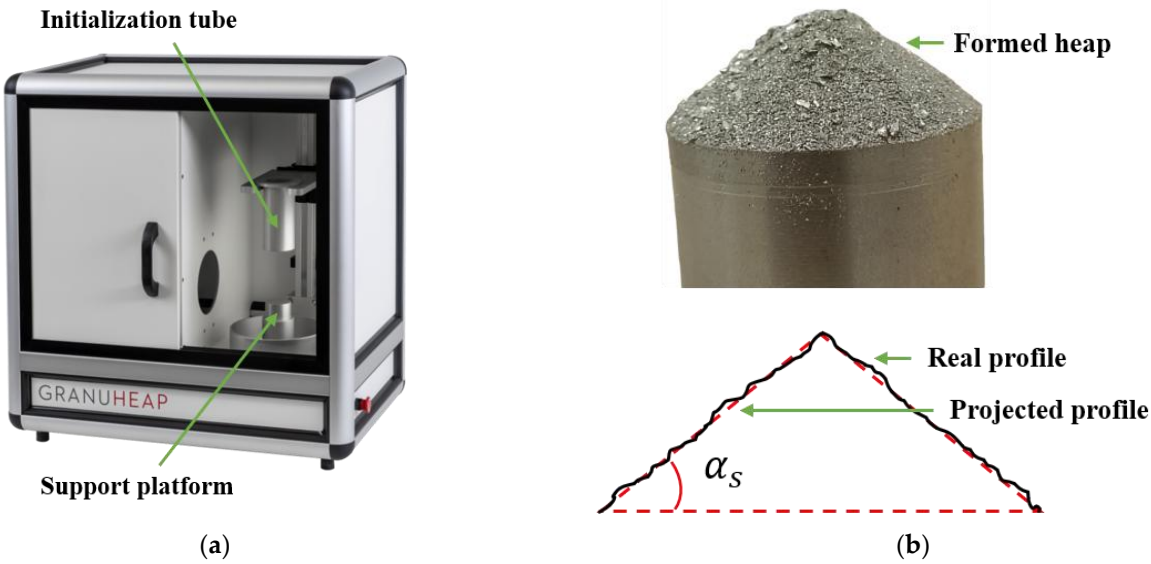

Figure 6. (**a**) GranuHeap device [28]; (**b**) example of a powder pile photograph and principle of identification of the static angle of repose α_S with the fitting of isosceles triangle.

2.3. Method for Characterizing Compressibility and Stress Transfer: A Quasi-Oedometric Compression Test

The mechanical properties of powders are evaluated by compression testing in a matrix assumed to be rigid, developed in the laboratory. The experimental protocol enables the determination of several powder parameters: the apparent elastic modulus E_p of the consolidated powder bed, the lateral stress transmission coefficient β_p (Janssen-like) and the wall–powder friction coefficient μ_p governing stress mobilization at the container interface.

The compaction setup consists of a tubular 440C stainless-steel die with an inner radius of 8 mm and a wall thickness of 10 mm. Two coaxially aligned and independently movable punches slide within the die (see Figure 7). The space between the punches defined the compression chamber with an effective height of 25 mm. For each test, the initial powder filling height H_0 is set to 22 mm. This setup is installed directly on the static lower plate of an electromechanical testing machine (MTS criterion C45 (Westerville, OH, USA)). The machine crosshead, which carries the 100 kN load cell, is removably attached to the upper punch to apply and measure the axial load. An LVDT sensor continuously measures the distance between the two punches, providing the height H_p of the consolidated sample inside the die. The load cell of the testing machine (Instron, 100 kN (Norwood, MA, USA)) records the axial force $F_{z\,up}$ applied to the top surface of the powder bed, while an additional 45 kN load cell (LLB 450 from FUTEK (Irvine, CA, USA)) positioned beneath the lower punch measures the axial transmitted force $F_{z\,down}$. The lower punch therefore only moves by a negligible amount corresponding to the deformation of the lower load cell. Four pairs of strain gauges (longitudinal and orthoradial) are bonded to the outer lateral surface of the tubular die at mid-height of the compression chamber. All gauges are wired in a quarter-bridge Wheatstone configuration, and each gauge orientation is selected to compensate for potential measurement errors arising from slight misalignment with the loading axis. Signals from the strain gauges, the LVDT, both load cells,

and the displacement of the upper punch connected to the testing machine were continuously recorded on a PC using LabVIEW 2015 SP1 ®, with the testing machine operating at a constant crosshead speed of 2 mm/min and data acquisition performed at 20 Hz.

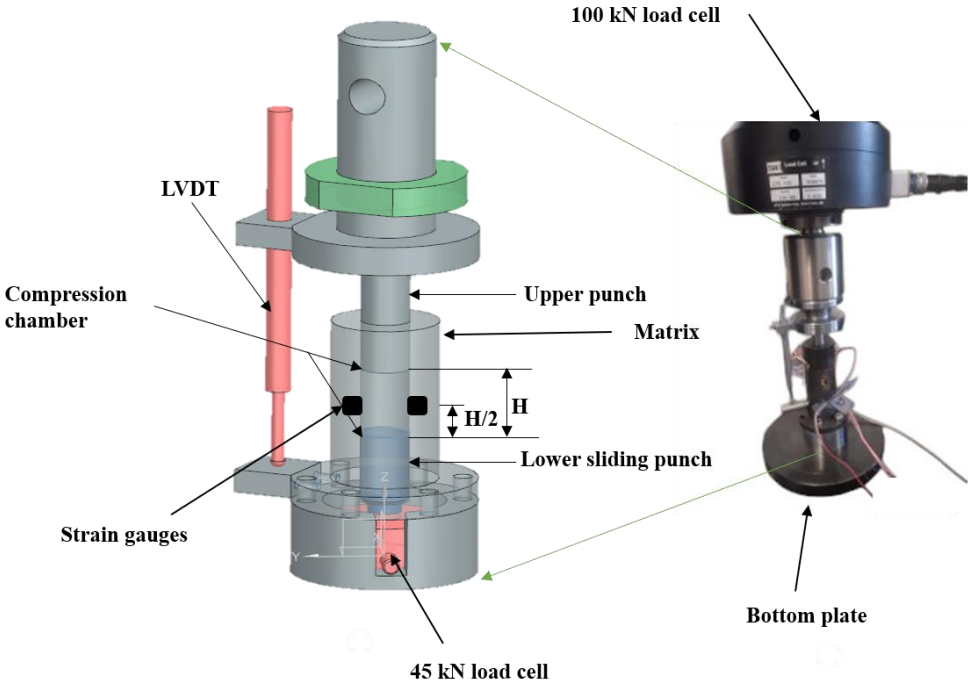

Figure 7. Rigid matrix compression assembly: (**left side**) CAD model, (**right side**) assembly positioned between the stationary bottom plate and the force sensor attached to the moving crosshead of the electromechanical testing machine.

Some calibration and validation tests were carried out preliminarily. Firstly, the compression test of the empty die between two rigid platens (0–30 kN) verified the proper functioning of the strain gauges and characterized the mechanical behavior of the die without any powder. From this test, a coefficient relating the longitudinal applied force to the gauge's strains was determined, which is used to estimate the portion of strain caused solely by powder–die friction. Secondly, a powderless test of the device was performed, placing the upper punch in contact with and compression against the lower sliding punch within their elastic range inside the die. It confirmed gauge sensitivity, with axial gauges recording ±5 μdef and ortho-radial gauges showing no measurable strain.

The apparent elastic modulus E_p of each sample is determined by calculating the ratio of the applied axial compressive stress $P_{z\,up} = \frac{F_{z\,up}}{S_b}$ over the current axial deformation of the powder inside the matrix ε_p (Equation (5)):

$$E_p = \frac{P_{z\,up}}{\varepsilon_p}\ (\text{MPa})\ \text{with}\ \ \varepsilon_p = \frac{H_p - H_0}{H_0}\ (\text{w.u}) \quad (5)$$

With H_p standing for the current height and H_0 for the initial height, before compaction ($\simeq$ 22 mm). The exact H_0 is determined by detecting the contact with the upper punch (i.e., when the load cell measures an increase by 10 N of the measured applied force $F_{z\,up}$ (Figure 8)).

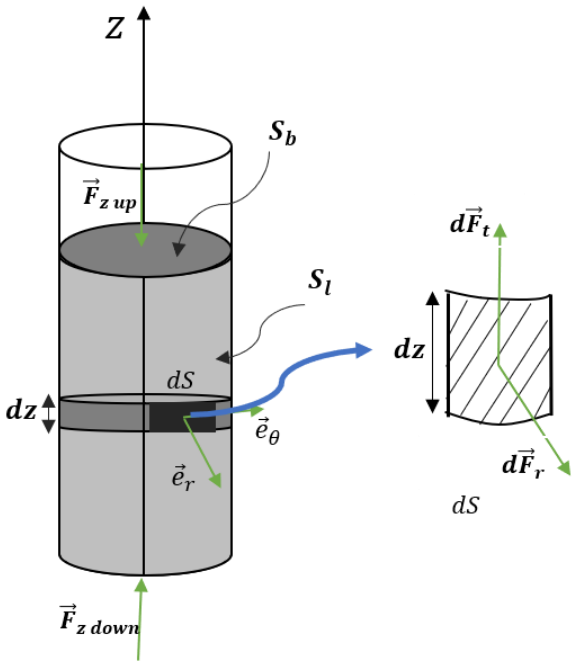

Figure 8. Schematic representation of the forces acting on the powder compact under compression, including radial ($d\vec{F}_r$) and tangential ($d\vec{F}_t$) forces exerted on a lateral surface element in contact with the die wall.

In the following, the powder/wall friction coefficient μ_p and the radial stress transmission coefficient β_p are inferred from these measurements. The subsequent paragraphs present the adopted model.

The forces acting on the powder compact are shown schematically on Figure 8. $\vec{F}_{z\,up}$ and $\vec{F}_{z\,down}$ are respectively the force applied by the downward upper punch and the resultant force at the bottom of the die applied by the lower sliding punch. These forces are applied over a section S_b and disc with radius r_0. $d\vec{F}_r$ and $d\vec{F}_t$ are respectively the infinitesimal radial force element and the infinitesimal tangential force element acting on a lateral surface element dS. Assuming a quasi-static test, the equilibrium of forces projected onto the vertical axis $\vec{z}$ is written as Equation (6).

$$F_t = \int_{S_l} dF_t = F_{z\,up} - F_{z\,down} \ (kN) \tag{6}$$

F_t is therefore the integral of the tangential forces directed along $\vec{z}$. The friction coefficient μ_p, assumed constant over the whole lateral surface S_l, is defined as

$$\mu_p = \frac{F_t}{F_r} \ (w.u) \tag{7}$$

Here, F_r is not strictly a force, with an application point and a given direction. By expressing the different terms in pressure, we obtain the Equation (8):

$$\begin{cases} F_t = (P_{z\,up} - P_{z\,down})S_b \\ F_r = \int_{S_l} P_r \, dS \end{cases} \ (kN) \tag{8}$$

P_r is the intensity of the pushing stress dF_r, applied by the powder radially on each infinitesimal lateral surface element dS. Combining Equations (7) and (8) gives the expression for the friction coefficient:

$$\mu_p = \frac{r_0}{2H_p} \frac{(P_{z\,up} - P_{z\,down})}{P_r} \ (w.u) \tag{9}$$

The pressure transmitted radially to the wall is quantified by a transmission coefficient β_p, assumed to be constant along the height of the compact [38] and defined by the relationship (10), with Pz the axial stress exerted on an infinitesimal slice (width dz) of powder located at height z.

$$\beta_p = \frac{P_r}{P_z} \quad (w.u) \tag{10}$$

The radial stress P_r can be obtained by measuring the strain thanks to the gauges installed at half of the initial filling height H_0. The radial stress is estimated by writing the mechanical equilibrium in the radial direction of a slice of the tubular matrix, with an infinitesimal height dz, in contact with the powder on the inside and free of contact on the outside.

$$P_r\left(\frac{H_0}{2}\right) = -\frac{E(\varepsilon_o - \nu\varepsilon_a)(r_0^2 - r_1^2)}{2(1-\nu^2)r_0^2} \quad (MPa) \tag{11}$$

Here, E and ν are the elastic parameters of the steel matrix, r_0 and r_1 are the inner and outer radii of the cross section, ε_o and ε_a are the ortho-radial and axial strains caused by the outward radial stress P_r. ε_o and ε_a are inferred from strain gauge measurements, from which components related to axial compression of the matrix due to vertical friction on the inner wall of the matrix are subtracted.

The vertical stress P_m is evaluated using Janssen's Slice Method, originally proposed in 1895 [39] and later refined by J. W. Strutt in 1912 [40] in order to elucidate the phenomenon of grain silo bursting. Janssen's analysis models the granular assembly as a series of thin horizontal slices. Examining an infinitesimal slice located at mid-height $\frac{H_0}{2}$ (see Figure 9), this method enables the axial stress P_m to be expressed as a function of the applied stress $P_{z\,up}$ by the upper downward punch and the reaction axial stress $P_{z\,down}$ by the lower punch (i.e., at the base of the compression chamber). P_m is defined as in Equation (12) because we assume that the axial stress distribution follows a non-linear, exponential profile, as predicted by Janssen's theory for grain silos.

$$P_m = \sqrt{P_{z\,up} \cdot P_{z\,down}} \quad (MPa) \tag{12}$$

It is therefore possible to evaluate the radial transmission coefficient β_p in $z = \frac{H_0}{2}$ as follows:

$$\beta_p = \frac{P_r\left(\frac{H_0}{2}\right)}{P_m} \quad (w.u) \tag{13}$$

The stress transmission coefficient describes the efficiency of axial-to-radial stress redirection in a confined powder bed and reflects factors such as particle size, shape, and mobility. In this study, we focus on how particle size and polydispersity influence this coefficient—and therefore the instantaneous wall stress state—rather than on their consequences such as the cumulative evolution of radial and hoop strain during long-term cycling.

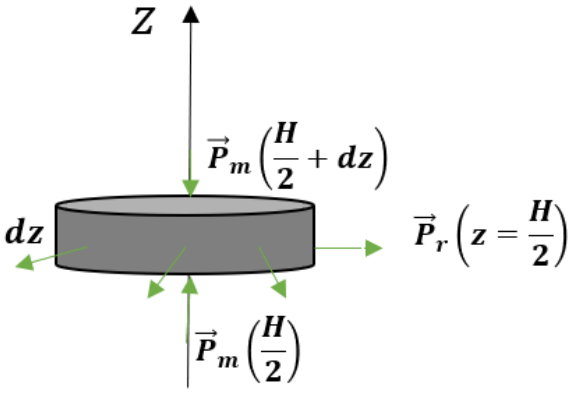

Figure 9. Stresses exerted on a powder layer of height dz, located at a vertical coordinate $z = \frac{H_0}{2}$ inside the compression chamber.

Assuming that compression at a rate of 2 mm/min is quasi-static, the longitudinal stress σ_t on the lateral wall can be expressed as a function of the difference between the applied force and the force measured at the bottom of the die ΔF_z, as well as the lateral surface area S_l:

$$\sigma_t = \frac{\Delta F_z}{S_l} \quad (\text{MPa}) \tag{14}$$

where $\Delta F_z = F_{z\,up} - F_{z\,down}$ and $S_l = 2\pi r_0 H_p$, H_p is the current height of the powder in the die.

To facilitate comparison of data from different powder batches, it is important to represent quantities as a function of the solid fraction ϕ. The solid fraction ϕ quantifies the powder compactness, and it is defined as the ratio between the volume of solid material and the total volume occupied by the powder; we can also write it as the ratio between the apparent density of the powder and the density of the solid material.

$$\phi = \frac{V_p}{V_{total}} = \frac{m/\rho_p}{\pi {r_0}^2 H_p} \ (\text{w.u}) \tag{15}$$

where m is the mass of powder in the die, $V_{total} = \pi r_0^2 H_p$ is the total powder filling volume in the die and $V_p = m/\rho_p$ is the volume of the intermetallic material contained in the die.

The mechanical properties are plotted as a function of the reduced solid fraction ϕ_r, defined as the difference between the current solid fraction ϕ and the initial solid fraction ϕ_0, prior to any compression $\phi_r = \phi - \phi_0$. The initial solid fraction ϕ_0 is determined for each powder from the known sample mass m and the measured initial height H_0, which may differ from the nominal target height (≈22 mm) due to surface non-planarity or measurement uncertainties. By reporting results as functions of the relative solid fraction ϕ_r, the influence of the initial packing variability is effectively minimized, allowing the analyses to focus on the intrinsic compaction behavior.

Three samples of each powder P_i, with i = {1,2,3,4,5}, were tested to assess the repeatability of the results. A progressive, stepwise cyclic compression protocol (0-10-0-20-0-30-0 kN) was applied to characterize the elastic response of the powders and their ability to transfer stresses to the die walls. To ensure a comparable initial filling height within the compaction cell, the following powder masses were used: 10.4 g for P1, 13.3 g for P2, 14.8 g for P3, 14.85 g for P4 and 16.8 g for P5.

3. Results

All tests on the various devices and for the different powder samples were conducted three times. The results presented in the following are the means and standard deviations of the values obtained for these three tests.

3.1. Dynamic Solicitations: GranuDrum

Figure 10a,b show the dynamic angle of repose θ and the cohesive index CI obtained from tests carried out on the five powders P1 to P5. One can see that all angles increase with the stabilized rotation speed of the drum. The avalanche phenomenon, which occurs at speeds below 10 rpm, prevents reliable interpretation of the curves. If we compare only quasi-monodisperse powders, between 10 and 35 rpm, fine powders tend to have higher flow angles than those consisting of coarser particles. For mixed powders, the quasi-bidisperse sample P4 has a higher angle than the polydisperse powder P5. For speeds above 35 rpm, the differences become insignificant. The P2 and P3 powders, which are quasi-monodisperse and larger in size, therefore exhibit Newtonian behavior because their cohesive indices vary very little with the rotation speed. Meanwhile, the fine powder P1, which is slightly more polydisperse than P2 and P3, and the mixed powders P4 and P5 exhibit shear-thickening behavior because their cohesion indices increase with the rotational speed [41].

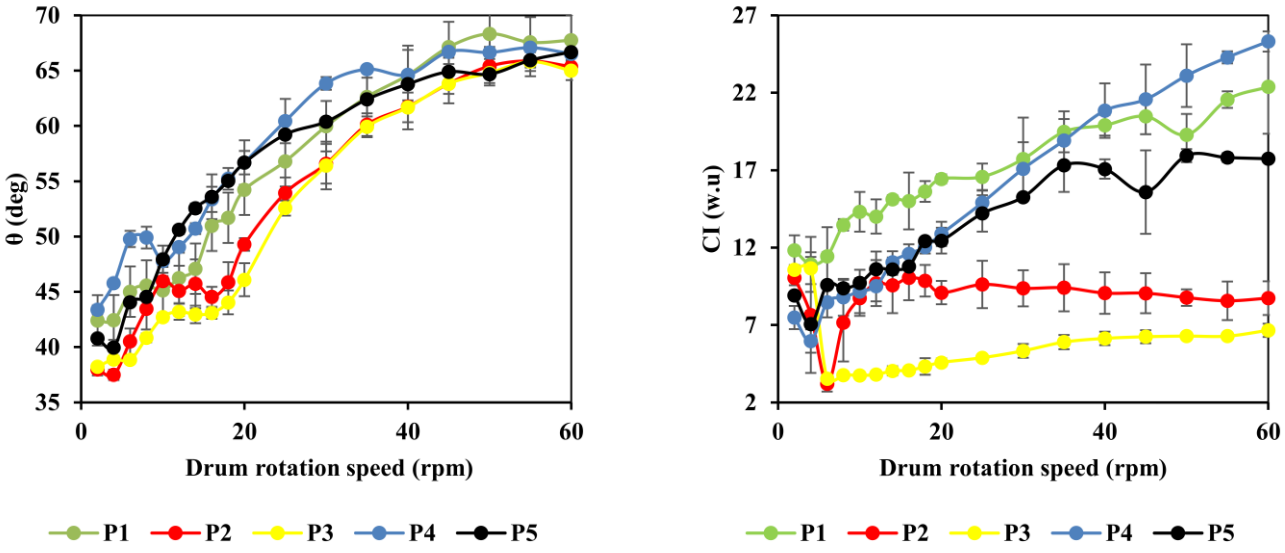

Figure 10. Flowability characterization curves for the five powder batches as a function of the rotation speed applied on the GranuDrum: (**a**) Dynamic angle of repose θ; (**b**) cohesive index CI and their standard deviations.

3.2. Quasi-Static Solicitation: GranuPack

Quasi-static settling tests were conducted on the five powders. The sample masses required to reach a filling volume of 35 mL in the cylindrical tube were 108 g for P1, 118 g for P2, 115 g for P3, 135 g for P4, and 128 g for P5. Figure 11 shows the powder bulk density as a function of the number of taps. The quasi-monodisperse powders exhibit lower initial and stabilized densities than the mixed powders. This behavior is attributed to the ability of fine particles to fill the interstitial voids between larger particles, thereby increasing the bulk density. The quasi-monodisperse batches P2 and P3 densify rapidly under tapping, whereas batches P1, P4, and P5 densify more slowly but ultimately to a greater extent.

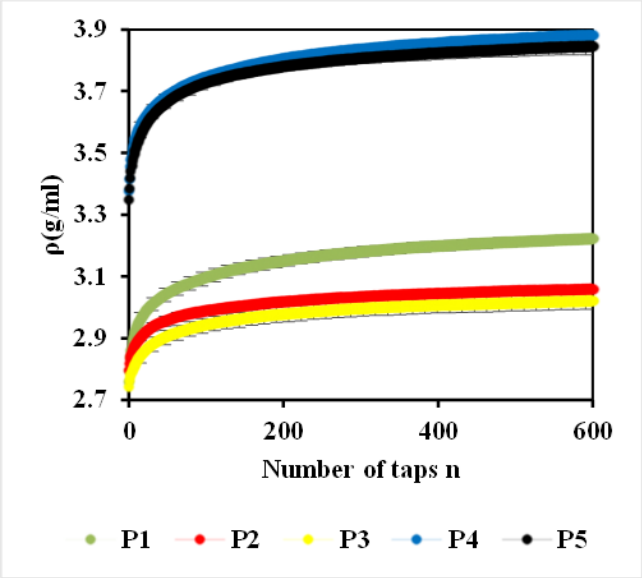

Figure 11. Bulk density ρ as a function of the number of taps n on the sample measured with the GranuPack instrument.

Figure 12 represents the Hausner ratio (Hr), the Carr Index (C), the characteristic tap number $n_{1/2}$ and the mobility index (α), all determined from the curves in Figure 11. According to Figure 12a, both Hr and C decrease as the mean particle size increases. The most polydisperse powders, P4 and P5, exhibit ratios and indices comparable to those of the fine powder P1, also moderately dispersed. This raises the question of whether the finest particles govern the behavior of mixed powders or whether these elevated Hr and C values primarily arise from polydispersity. In Figure 12b, the characteristic tap number $n_{1/2}$ increases with the particle size for powders P1, P2, and P3. Furthermore, the mixed powders (P4 and P5) have $n_{1/2}$ values similar to those of the fine powder P1. The mobility index α is high (>15) for strongly polydisperse samples but remains moderate (<10) for quasi-monodisperse samples. These trends indicate that the packing ease is primarily governed by the average particle size whereas the settling rate is more sensitive to the dispersity.

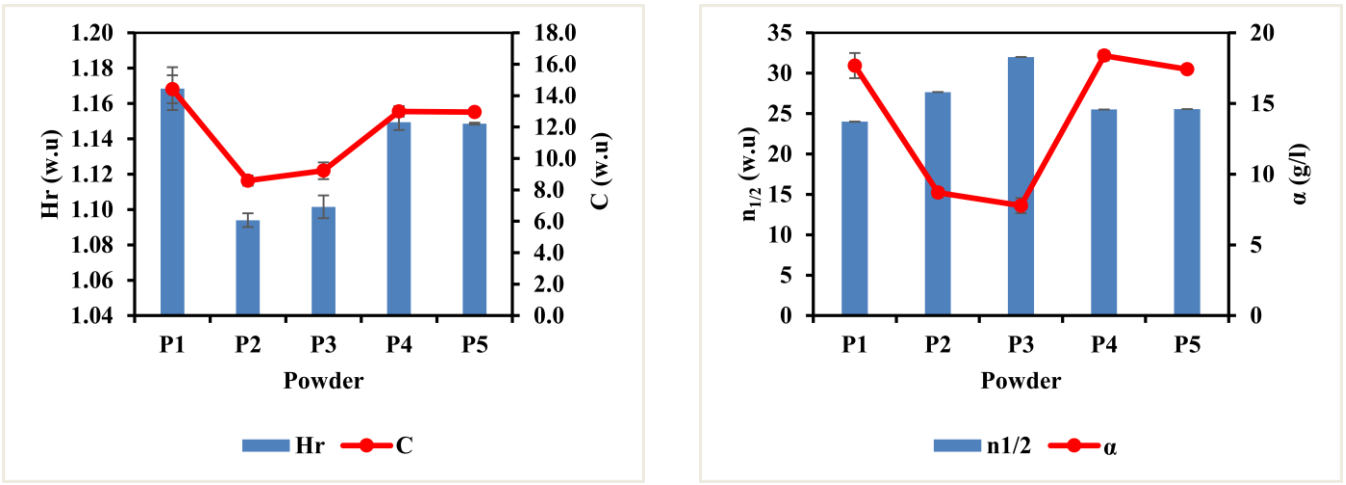

(**a**) (**b**)

Figure 12. Settling ease indicators for each powder batch inferred from Figure 11: (**a**) Hausner ratio Hr, Carr Index C; (**b**) characteristic tap number $n_{1/2}$ and mobility index α describing the settling dynamics.

3.3. Static Equilibrium Configuration: GranuHeap

The conical powder heaps obtained on the GranuHeap device represent an equilibrium of a particulate medium under the action of internal friction, internal cohesion, and gravity. Figure 13 shows images captured when the heaps reached stability. The values of the static angles of repose α_s, which correspond to the base angles of isosceles triangles fitted to the average contours of the obtained heaps, are shown in Figure 14. A classic evolution of the angles as a function of the particle size is observed: powders with fine particles have the largest angles (P1: 51 deg), while those with coarser particles have the smallest angles. The polydisperse samples P4 and P5 behave similarly to P1, with the finer particles governing their stabilization.

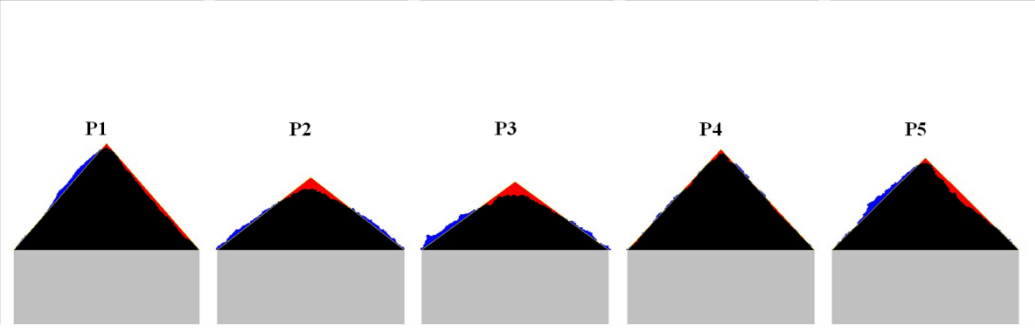

Figure 13. Piles from different powder batches obtained using the GranuHeap device.

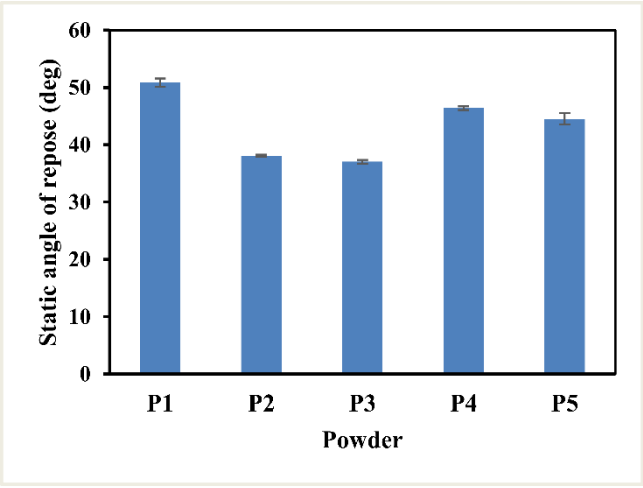

Figure 14. Static angles of repose α_s values of the triangle fitted on the average heap's contours determined with GranuHeap.

3.4. Characterizing Compressibility and Stress Transfer by Quasi-Oedometric Confined Compression Tests

For each powder, the compression force $F_{z\,up}$ and the force transmitted to the bottom of the die $F_{z\,down}$ are measured and plotted as a function of the deformation of the compact ε_p, as shown in Figure 15a. ΔFz is the difference between the applied force and the transmitted force. Two phenomena combine to lead to a non-linear curve when force is applied: the rearrangement of particles and their compression. Discharges are prescribed in order to observe the elastic relaxation of the bed, but it cannot be ruled out that rearrangements also occur during discharge. After each unloading from the imposed forces of 10 kN, 20 kN, and 30 kN, considerable permanent deformation is observed, which can be attributed mainly to rearrangement. It is also possible that fragmentation of the particles under stress occurs. The shape of the ΔFz curve is interesting. To interpret it, it is

important to note that compression assembly validation tests were conducted without powder, prior with no axial contact and then with punch against punch. The result is that punch–wall friction is negligible compared to the forces involved and that without powder, the transmission of force is complete: $F_{z\,up} = F_{z\,down}$ and $\Delta F_z = 0$.

For compression tests of all powders, during each discharge, ΔF_z rapidly changes sign, then gradually decreases to reach almost 0 kN at the end of each discharge. ΔF_z, being the force transmitted by the die walls, can be attributed to friction on the inner lateral surface and thus qualified by the friction coefficient μ_p defined in Equation (9). It is also possible that "arches" form through successive locking of adjacent particles, acting as keystones at different heights of the bulk and limiting the transmission of axial forces to the lower layers. One would therefore focus instead on the stress transmission coefficients β_p described in Equation (13), which cover both phenomena. In both cases, to determine μ_p or β_p, it is necessary to examine the axial and ortho-radial strains of the tubular die (Figure 15b). The intensity of these strains is low (<100 μdef), which confirms the rigidity of the die. The return to zero confirms that the die material is solicited within its elastic range. The curves are not linear and do not overlap completely due to the non-linearity of force transmission. As expected, the ortho-radial deformations are positive: there is a slight elastic increase in the outer hoop circumference due to the inner thrust of the powder. Longitudinal deformations are negative because they result both from the effect of the radial thrust of the powder on the inner wall P_r (which would have a positive impact) and from the compression of the die under the effect of the axial transferred force ΔF_z (which has a negative impact most of the time, except by the end of unloading). This interpretation is confirmed by compression tests on a lubricated elastomer ($\nu = 0.5$ and negligible friction) that does not cause negative longitudinal strain.

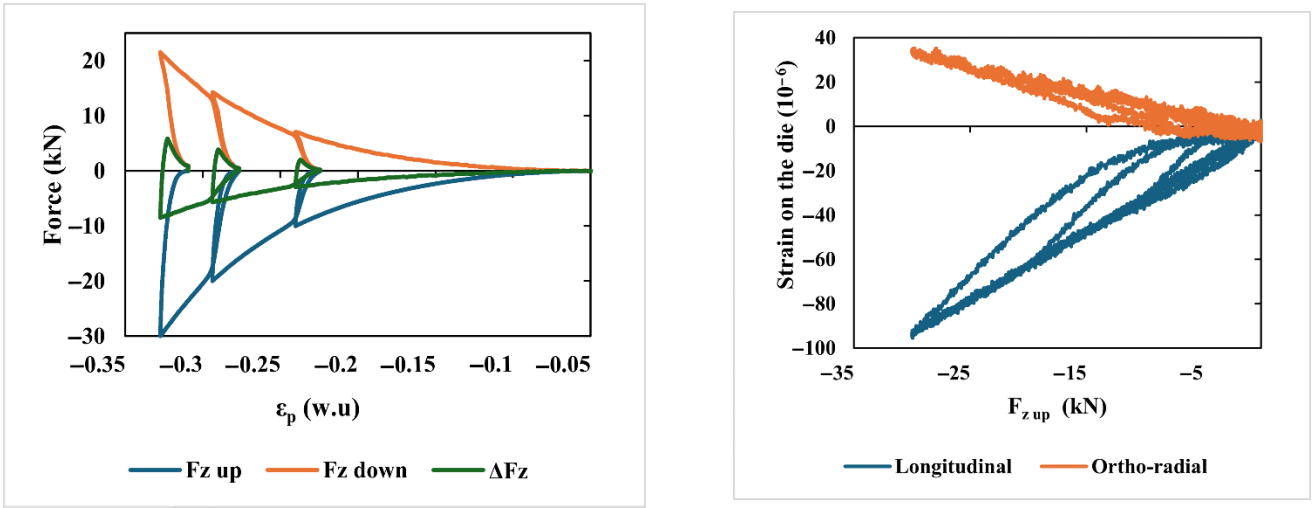

(**a**) (**b**)

Figure 15. (**a**) Axial forces involved depending on powder compaction ε_p: $F_{z\,up}$, applied force; $F_{z\,down}$, measured force transmitted to the bottom of the die; ΔF_z, difference between the applied and transmitted forces transferred via the wall to the die; (**b**) ortho-radial and longitudinal strains of the die, computed from the average of the measurements of the four strain gauges attached to the outer surface of the die.

Using the model presented in Section 2.3, and in particular Equations (11) and (14), we can calculate the stresses exerted by the powder at mid-height on the inner wall. The radial stress P_r and the mean longitudinal stress σ_t are plotted in Figure 16. The positive longitudinal stresses at the end of the discharges reveal the tensile state of the matrix. This

may be due either to upward friction during the elastic release of the powder or to the formation of inverted arches.

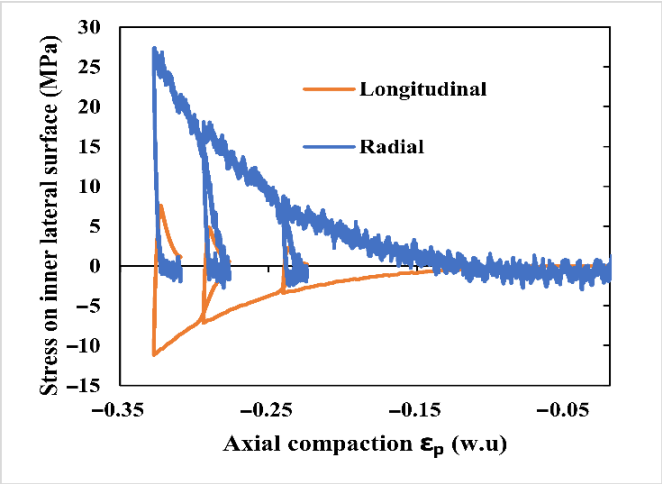

Figure 16. Example of radial and longitudinal stresses applied to inner lateral surface of the matrix by the powder P1 during loading and unloading cycles.

3.4.1. Elastic Behavior Analysis

Figure 17 displays the apparent elastic modulus (from Equation (5)) as a function of the reduced packing fraction ϕ_r. For readability reasons, quasi-monodisperse powders P1, P2 and P3 are plotted in Figure 17a, and bidisperse P4 and polydisperse P5 powders are plotted in Figure 17b. There is an increase in the apparent elastic modulus E_p with the packing fraction ϕ_r, i.e., the densification of the medium. The validity of the curves over the entire test sequence is questionable due to the rearrangement of particles combined with the elastic compaction of the medium during loading. This is why we focus our observations on the values of the modulus at the very beginning of the elastic unloading, i.e., when the force $F_{z\,up}$ is 10 kN in cycle 1, 20 kN in cycle 2, and 30 kN in cycle 3.

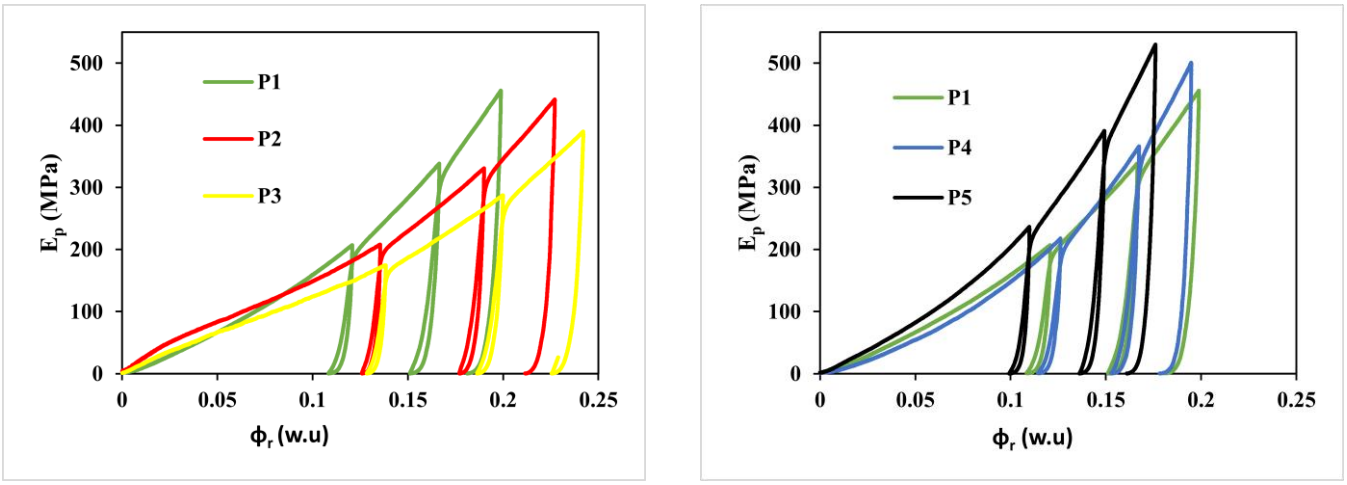

(**a**) (**b**)

Figure 17. Apparent elastic modulus E_p of the powder-consolidated bulk in the compression die as a function of the reduced packing fraction ϕ_r: (**a**) quasi-monodisperse powders P1, P2, and P3; (**b**) polydisperse powders P4 and P5, compared to P1.

Figure 18 and Table 2 present the values of the apparent elastic moduli E_p evaluated at the beginning of each elastic unloading. For quasi-monodisperse powders (P1 to P3),

the finer the granularity, the greater the modulus. For mixed powders P4 and P5, even though their median particle size is between that of P2 and P3, their apparent elastic moduli are the highest because they contain P1 powder in their mixture. It can also be said that the higher the polydispersity, the greater the apparent stiffness, and the faster it increases with the applied force.

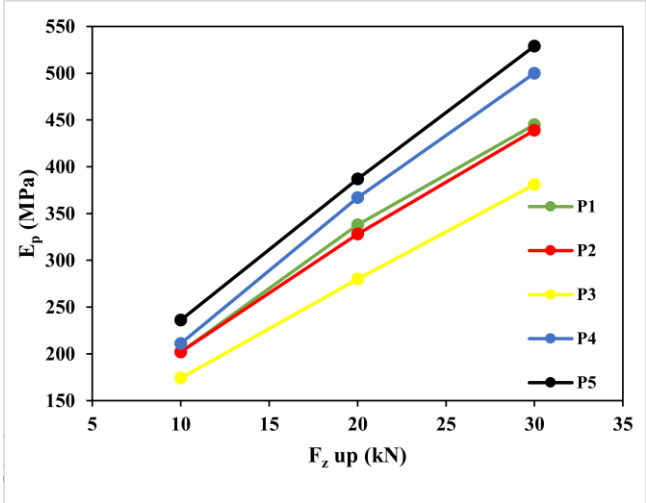

Figure 18. Apparent elastic moduli E_p evaluated at the beginning of elastic unloading at 10 kN, 20 kN and 30 kN.

Table 2. Values of the apparent elastic moduli E_p evaluated at the beginning of elastic unloading.

Powder	D50/Median (µm)	Polydispersity	Modulus at 10 kN (MPa)	Modulus at 20 kN (MPa)	Modulus at 30 kN (MPa)
P1	154.66	High	202 MPa	338 MPa	445 MPa
P2	522.50	Moderate	202 MPa	328 MPa	439 MPa
P3	1074.92	Moderate	174 MPa	280 MPa	381 MPa
P4	662.31	High	211 MPa	367 MPa	500 MPa
P5	507.53	Very High	236 MPa	387 MPa	529 MPa

3.4.2. Coefficients of Friction and Stress Transmission

The friction coefficients μ_p of the quasi-monodisperse powders P1, P2, and P3, and the quasi-bidisperse (P4) and polydisperse (P5) powders are shown in Figure 19. The raw μ_p data may exhibit strong fluctuations possibly due to transient particle rearrangements. To extract the underlying trend, a moving average over 100 consecutive points (smoothing window spans ≈ 0.002, less than 1% of the total domain) was applied. These fluctuations are mainly due to unavoidable noise from the strain gauge measurements used to calculate Pr, which is present in the μ_p Equation (9). The curves are therefore not reliable when strains are small, for packing fractions below 0.05. However, Figure 19a shows that the finer the powder, the higher the powder–wall friction coefficient. One should note that this coefficient decreases with the compaction of the powder sample for quasi-monodisperse powders. For the polydisperse powder, the friction coefficient seems to increase with compaction. Its values are lower for the mixed powders and the most polydisperse powder P5 has the lower coefficient on the first part of the compression test. When the packing fraction is higher, the curves all seem to converge toward a value close to $\mu_p \approx 0.4$.

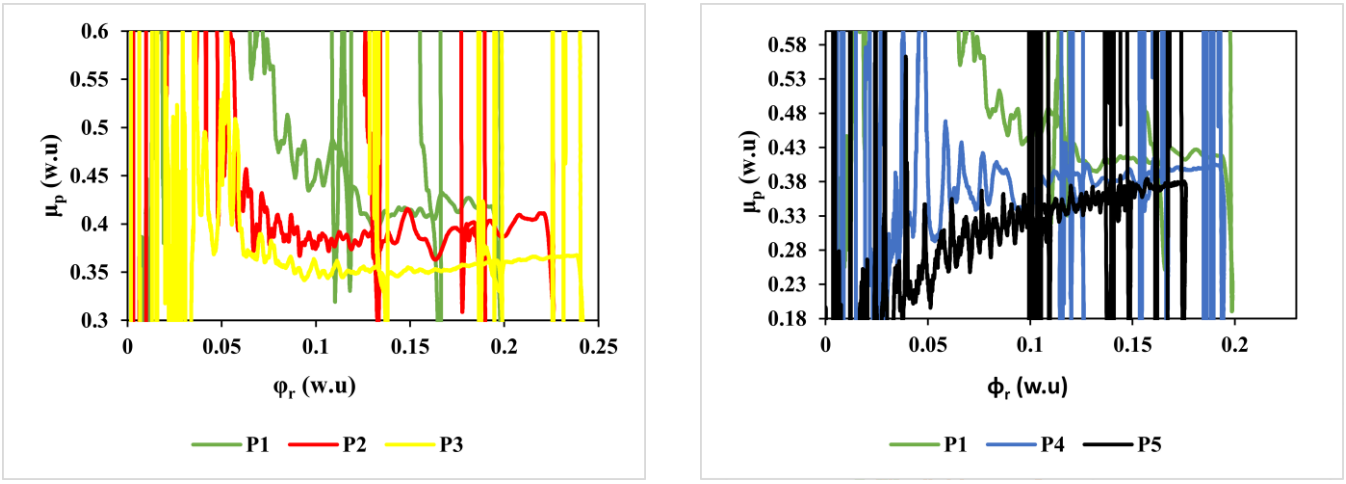

(**a**) (**b**)

Figure 19. Coefficient of friction on the matrix μ_p: (**a**) powders P1, P2, and P3; (**b**) powders P1, P4, and P5.

The values of the powder/wall friction coefficients for compressed powders for loads of 20 kN and 30 kN are listed in Table 3.

Table 3. Ranking of powder/wall friction coefficients of compressed powders for loads of 20 kN and 30 kN.

Ranking ↓	D50/Median (μm)	Polydispersity	Friction Coef. at 20 kN	Friction Coef. at 30 kN
P1	154.66	High	0.42	0.41
P4	662.31	High	0.41	0.41
P2	522.50	Moderate	0.39	0.40
P5	507.53	Very High	0.37	0.38
P3	1074.92	Moderate	0.35	0.37

The stress transmission coefficients β_p are plotted for forces applied at 10 kN, 20 kN, and 30 kN in Figure 20. The different curves show significant differences at the start of compression but tend toward similar values toward the end of compression. For quasi-monodisperse powders, the P2 and P3 curves, which are the coarsest, are consistently above that of P1. The mixed powders P4 and P5 have transmission coefficients higher than all quasi-monodisperse powders; P5 has the highest coefficients.

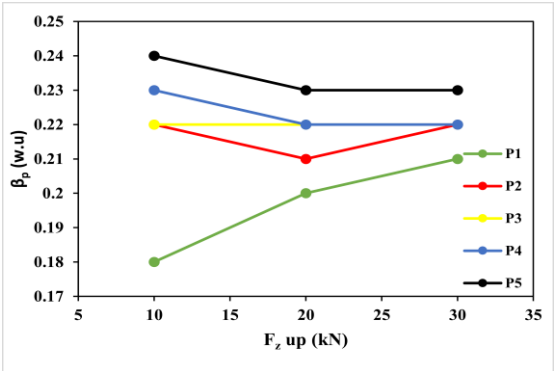

Figure 20. Values of radial stress transmission coefficients β_p for powders P1 to P5 for applied forces of 10, 20, and 30 kN.

4. Discussion

4.1. Dynamic Solicitations: GranuDrum

The dynamic flow behavior in the GranuDrum device is influenced simultaneously by friction between particles and cohesive forces. The cohesive index CI gives a measure of the macroscopic cohesion of the powder, i.e., at the flow scale, allowing ranking of the powders. This ranking is shown in Table 4. As expected, the finer the powders, the more cohesive they are, which prevents them from flowing freely. The behavior of polydisperse powders is governed by that of the finest particles they contain and are therefore also cohesive. The evolution of the cohesion index CI as a function of the rotation speed (Figure 10b) for P1, P4, and P5 reveals shear-thickening behavior, while P2 and P3 exhibit quasi-Newtonian behavior. A cross-interpretation of Figure 10a and the cohesion classification suggest that internal friction in P1 is less pronounced than in P4 and P5. P2 and P3 have a comparable dynamic angle of repose θ but are much less cohesive, and therefore have more significant internal friction.

Table 4. Ranking of powders according to their interparticle friction properties and internal cohesion based on GranuDrum measurements, under dynamic solicitations.

Ranking ↓	Cohesion	Interparticle Friction
1	P1	P3
2	P4	P2
3	P5	P5
4	P2	P4
5	P3	P1

For these interpretations, we limited our analysis to the rotational speed range [10; 35] rpm in order to avoid biases related to avalanches occurring at low speeds and biases related to particle segregation in polydisperse samples occurring at high speeds. Indeed, as shown in Figure 21 for powder P4, particle segregation depending on size increases as the drum rotation speed increases, with fine particles remaining in the center, where the dynamic angle of repose θ is evaluated. This may partly explain why the curves of the dynamic angle of repose of powders P4 and P5 approach that of P1 for speeds above 35 rpm.

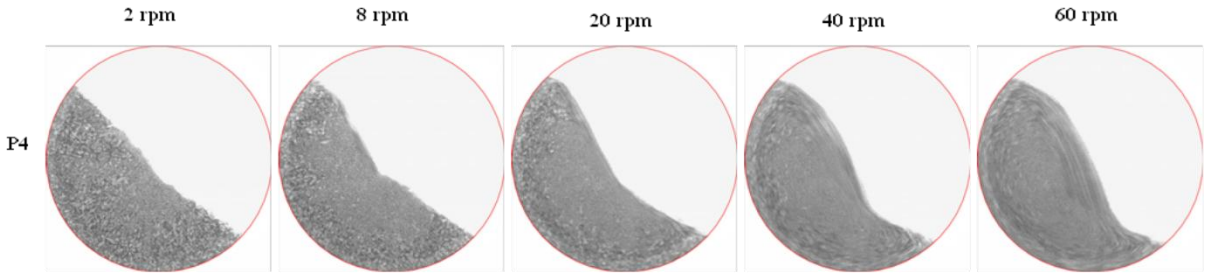

Figure 21. Evidence of segregation of P4 powder during characterization in the rotating drum.

For the application under consideration of solid hydrogen storage through the reversible hydriding of particles, friction between particles and internal cohesion are the variables to be considered in order to understand the ease of particle movement and stress transmission during respiration (swelling/shrinkage of the bed during H_2 absorption/desorption cycles). In the literature, it is stated that cohesion in the powder bed limits movement between particles and promotes increased stress [42], but also that friction between particles promotes higher stress transmission [43]. This is consistent with our observations as coarse powders P2 and P3 enable stress transmission because their behavior is

governed mainly by friction, while fine powder P1, which has stronger internal cohesion, like mixed powders P4 and P5, promotes transmission of these stresses through both friction and cohesion.

4.2. Quasi-Static Solicitations in GranuPack and Static Solicitations in GranuHeap

The criteria established by Hausner and Carr [36,37] establish a link between the values of Hr and C and the ease with which a powder flows. According to this criterion, powder P1 (Hr = 1.17, C = 15) has good free flowability, well above that of cohesive materials such as lactose [34], but P1 remains the most cohesive powder batch in this series of samples. Batches P4 and P5, which have ratios and indices similar to P1, also show good free flowability and a level of cohesion comparable to that of P1, suggesting that the small grains present in P1, but also in mixtures P4 and P5, govern the cohesion of all the mixtures. The coarser powders P2 and P3 have excellent flowability, with lower ratios and indices (Hr = 1.09, C = 6), indicating weaker cohesion compared to batches P1, P4, and P5. Powders P1, P4, and P5 have a characteristic tap number $n_{1/2}$ between 24 and 25, while large powders P2 and P3 have numbers between 28 and 32. Conversely, for the mobility index α, the values for P1, P4 and P5 are the highest, between 17 g/L and 19 g/L, while P2 and P3 are between 14 g/L and 15 g/L. This means that, beyond the initial or final bulk density itself, powders P1, P4, and P5 pack more easily and quickly than coarse powders P2 and P3. The rapid packing of P1, P4, and P5, which are more polydisperse, can be explained by the ability of fine particles to move easily by segregation to occupy the spaces available between coarse particles. In contrast, P2 and P3 grains, being coarser and more uniform, have less freedom to reorganize; thus, these samples require a greater number of impacts to achieve maximum compaction, which is also less variable.

These results allow for further differentiation of powder batches based on their flowability and reveal that the most cohesive batches also have the fastest packing. The results are summarized in Table 5, which ranks cohesion, flowability and packing speed in descending order.

Table 5. Ranking of powders regarding their cohesion and flowability based on the packing speed measured on GranuPack.

Ranking ↓	Packing Speed	Cohesion	Flowability
1	P1	P1	P2
2	P4	P4	P3
3	P5	P5	P5
4	P2	P3	P4
5	P3	P2	P1

The static angles of repose measured using GranuHeap should be interpreted considering the results of flowability and cohesion obtained with GranuPack. Table 6 lists the static angles of repose and relates them to the median particle size (D50) and the degree of polydispersity of the powder batches. The angles of repose are slightly dispersed and the contours of the piles are regular and almost conical in any case. It is observed that the batches forming the highest heaps are those containing the finest particles, which are also the most polydisperse blends. The angle of repose is driven by both interparticle cohesion and friction. Consequently, these results corroborate the cohesion ranking obtained previously (Table 5) while not allowing a clear decoupling of the respective contribution of cohesion and interparticle friction.

Table 6. Static angle of repose (GranuHeap) and the particle size and dispersity data of the powder batches.

Static Angle of Repose (deg)	Powder Batch	D50/Median (μm)	Polydispersity
33	P3	1074.92	Moderate
38	P2	522.50	Moderate
44	P5	507.53	Very High
46	P4	662.31	High
51	P1	154.66	High

To conclude this section, the results obtained in a quasi-static and static configuration confirm and complement our understanding of the dynamic tests performed on the GranuDrum. In this first part, our objective was to characterize how changes in particle size and polydispersity affect the powder's flowability, cohesion, and packing ability. Fine (P1) and mixed polydisperse (P4, P5) powders exhibit higher cohesion, greater resistance to flow, and shear-thickening behavior. In contrast, coarse-grained powders (P2, P3) are less cohesive, display excellent flowability, and have a quasi-Newtonian response to dynamic solicitations.

4.3. Quasi-Oedometric Confined Compression Tests

We showed in Section 3.4.1 that, during compression, the apparent elastic modulus increases with the decreasing particle size. Moreover, this increase becomes more pronounced for a higher level of polydispersity within the medium. This behavior can be explained by the fact that apparent elastic moduli are correlated with the density of compressed powders, and that bi- and polydisperse powder samples are both initially denser and undergo more rapid densification under compression.

It should be noted, however, that additional parameters such as particle shape or roughness may also affect this modulus, two characteristics that are particularly affected when decrepitation under dihydrogen occurs, whereas the present experiments were conducted exclusively in air, on batches that were all crushed in the same way. In the context of solid-state hydrogen storage, O. Gillia [44] reported that the stiffness of hydriding media increases as the particle size decreases, in agreement with J. Visser's findings [41] that fine powders exhibit stronger interparticle attractions, particularly Van der Waals forces, than coarse powders. Our results further show that mixing fine and coarse particles leads to an even stiffer granular medium than the initial quasi-monodisperse powders. This trend has also been identified in hydrogen storage systems, where O. Gillia [44] attributes the rise in mechanical stresses on the storage vessel to polydispersity-induced densification, itself promoted by the segregation of small fragments formed during cycling. Such cycling-induced fragmentation, or decrepitation, combined with settling has been shown to increase wall stresses in several studies, including Okumura et al. [22].

Overall, our experiments suggest that while particle fineness and size distribution both influence stress transmission to the vessel walls, polydispersity plays the more dominant role; this is consistent with the most recent studies conducted under hydrogen [27].

The coefficient of friction between the powder and the wall appears to be mainly influenced by particle size rather than polydispersity, when considering powders whose particles have similar morphologies, i.e., angular due to jaw crushing. Indeed, Table 3 indicates that the powders exhibiting the highest coefficients of friction are those containing a higher proportion of fine particles, while coarser powders interact less with the confining wall. This observation is consistent with the experimental study of C. Lanzerstorfer et al. [45] on various materials, which reported that the friction coefficients of Al_2O_3, $CaCO_3$, and SiC compounds are higher for fine powders and decrease with the increasing

particle size when compressed against a steel wall. Their results further demonstrate that the coefficient of coarse powders decreases more rapidly than those of fine powders, in agreement with the trends observed in the present study. This trend can be attributed to better distribution of powder–wall contacts for fine powders, leading to a more uniform mobilization of friction forces at the interface. Such an effect may result in increased stress levels, particularly in the lower region of the hydride storage tank, as fine particles are prone to downward segregation during the cyclic "breathing" of the hydride bed.

Contrary to the particle–wall friction coefficient, the radial stress transmission coefficient is higher for coarse particles and lower for fine particles. The radial stress transmission coefficient reaches its highest values for mixed samples, followed by quasi-monodisperse samples composed of the coarsest particles. This behavior may be related to the greater mobility of fine particles, which can hinder the formation of stable and effective load-bearing contacts. In contrast, coarse particles, owing to their larger size and surface asperities, may favor mechanical interlocking and enhanced stress transmission. Coarse particles could also be more prone to forming a preferential load path, sometimes described as "force chains" or "arching structures", that could act as load-bearing keystones. It would tend to redirect stresses toward the confining walls rather than to the powder layer located directly below. This interpretation is in accordance with the work of Y. Li et al. [43], who used discrete element modeling (DEM) of isotropic compressed granular materials with a controlled particle size and shape dispersion to investigate stress transmission mechanisms, and demonstrated that larger particles transmit stresses more efficiently. These observations suggest that, in solid-state storage vessel service life, during the "breathing" of the granular bed, as there is a progressive reduction in the mean particle size of the storage medium during successive absorption/desorption cycles [46], from an initially coarse and polydisperse powder to an increasingly fine and monodisperse one, the radial stresses exerted on the walls should be most intense during the early stage of cycling, followed by a gradual decrease. Previous published experimental studies on this subject [21,22,24,26,47,48], which monitored the cumulative plastic strain of the vessels using strain gauges, confirm the localization of the strain on the lower part of the walls but do not clearly report this subtle transient phenomenon of evolving stress transmission because the characterization techniques used do not provide insight into the interaction behavior of the powder itself during cycles. Recent work by G. Stahlkopf et al. [27] reinforces the justification of this interpretation. They investigated the development of internal radial forces in a vertical storage tank filled with an AB_2 alloy powder. By combining strain measurements obtained from strain gauges with synchrotron-based micro-computed tomography during cycling, together with SEM observations performed after cycling, they showed that the mechanical evolution strongly depends on the initial particle size distribution. When the powder is initially coarse, the early cycles induce particle fracture, generating finer fragments that migrate toward the bottom of the bed and become inserted between larger, unfractured particles. This process leads to a locally increased packing fraction in the absorption state, resulting in progressively increasing radial expansion stresses in the lower part of the vessel. Conversely, when the initially inserted powder already consists of packed monodisperse fine particles, the highest radial stress levels occur during the first few absorption–desorption cycles. Subsequent particle rearrangement then leads to a gradual reduction in the stress state.

5. Conclusions

In a solid-state hydrogen storage tank, metal powder particles expand and shrink, fracture, move, and segregate as reversible hydriding cycles repeat. With each absorption/desorption cycle, these phenomena cause stress on the walls of the tank. This stress intensifies throughout the cycles, mainly due to settling, and in some cases leads to plastic deformation and damage to the tank.

In this article, we propose an experimental characterization of both the flowability and compressibility of a $TiFe_{(1-x)}Mn_x$ ($x \approx 0.1$) powder, a common intermetallic storage medium, in order to qualify its ease of flow (movement of particles relative to each other), its mechanical properties, and its stress transmission properties (between particles and to the tank's walls). To simulate different stages of self-fracture under hydriding (i.e., decrepitation), an original crushed powder batch was sieved and blended to create five distinct powder samples. Thanks to three commercial devices (GranuDrum, GranuPack, and GranuHeap from GranuTools) and a laboratory-developed instrumented compression bench, the samples were tested under dynamic, quasi-static and static conditions, and under quasi-oedometric compression. This study provides key insights into the influence of particle size and polydispersity—both direct consequences of decrepitation—on flowability and stress transfer in solid-state hydrogen storage tanks.

- The dynamic flowability is governed by particle size and polydispersity: Fine powders (P1) and mixed powders (P4, P5) exhibit a shear-thickening behavior, with an increasing cohesive index as the rotational speed rises, whereas coarse powders (P2, P3) display a quasi-Newtonian response.
- Regarding cohesion and ease of packing: Fine and mixed powders (P1, P4 P5) are more cohesive and less free-flowing, yet they compact more readily under quasi-static loading. In contrast, coarse powders exhibit low cohesion and excellent flowability but are less prone to compaction, indicating that the fine particle fraction controls the overall cohesive behavior in mixed systems.
- Quasi-oedometric compression tests reveal that polydispersity strongly enhances the apparent stiffness of consolidated powders, exceeding the effect of particle fineness alone. Compression curves and force transmission to the die base and walls suggest a competition between wall friction and mechanism that may involve arch formation and mechanical interlocking. These possible arch-like load-bearing structures could also undergo a transient redistribution during the unloading stage.
- Powder–wall friction is primarily governed by particle size, with higher friction coefficients observed for powders rich in fine particles (P1, P4, P5), likely due to a more uniform distribution of powder–wall contacts, which may enhance stress levels in the lower regions of storage vessels through fine-particle segregation. In contrast, radial stress transmission (β_p) is enhanced by the presence of coarse particles (P2, P3), which promote mechanical interlocking and arch formation, thereby facilitating stress transfer toward the confining walls.

Based on these findings, the dominant mechanisms governing stress transmission are expected to evolve as follows throughout the solid-state storage tank's operational life. In the initial state, characterized by a coarse and quasi-monodisperse powder, stress transmission is primarily controlled by strong interparticle friction and efficient radial load transfer that may result from mechanical interlocking between particles. In the intermediate state, decrepitation induces a broader particle size distribution, leading to a marked increase in the apparent stiffness of the powder bed (E_p). This enhanced rigidity, together with the progressive increase in powder–wall friction (μ_p) associated with the generation of fine particles, becomes the predominant contributor to stresses exerted on the tank walls. In the late stage, following extensive cycling, the powder bed evolves toward a finer

and more segregated structure. Under these conditions, elevated internal cohesion and high powder–wall friction govern stress transmission, particularly in the densely settled lower regions of the tank. Although the overall stiffness of the powder bed decreases compared to the polydisperse state, stress transmission in this late stage is primarily governed by increased internal cohesion and enhanced powder–wall friction. Recent experimental observations of [27] appear consistent with these interpretations. It should be noted that the present conclusions are derived exclusively from experiments performed in air atmosphere and on mechanically milled powders. The possible evolution of particle morphology and surface roughness resulting from hydriding-induced fragmentation has not been considered, although it may significantly influence powder flowability and frictional properties via interfacial effects.

This study provides a clear, although simplified, model for the evolution of mechanical stress inside a hydride tank, while the idealized powder batches used in this study may not perfectly represent the progressive evolution inside a real tank. However, this experimental approach allows us to conjecture the main causes of the evolution of stress transmission when the medium decays and ages during cycling. In addition, it lays useful methodological foundations for establishing a numerical discrete element model (DEM) or digital twins to identify the behavior of a hydride in order to simulate ”breathing” and better represent the stresses exerted on the solid-state storage tank wall.

Author Contributions: Conceptualization, A.M. and D.C.; methodology, A.M. and C.N.Y.; validation, C.N.Y., A.M., T.J. and A.N.; formal analysis, C.N.Y.; investigation, C.N.Y., T.J. and A.M.; resources, A.N. and T.J.; data curation, C.N.Y. and A.M.; writing—original draft preparation, C.N.Y. and A.M.; writing—review and editing, C.N.Y., A.M. and D.C.; supervision, A.M. and D.C.; project administration, A.M.; funding acquisition, A.M. All authors have read and agreed to the published version of the manuscript.

Funding: This work has been supported by the EIPHI Graduate School (contract ANR-17-EURE-0002) and the Region Bourgogne Franche-Comté. This project is also partially funded by the French Ministry of Higher Education and Research (MESR), which finances the doctoral student’s scholarship. This work was partly supported by the French RENATECH network and its FEMTO-ST technological facility MIMENTO. The authors would like to also thank the AMETISTE platform (FEMTO-ST) for access to the equipment.

Data Availability Statement: The data that support the interpretations and conclusions of this study are available from the authors upon reasonable request.

Acknowledgments: Special thanks to Granutools in Awans, Belgium, for their hospitality and support during the flowability tests of our powder, which significantly contributed to this research. The authors also express their gratitude to Vincent Tissot for its help in the design and manufacture of the compression device. Additionally, sincere thanks are extended to MAHYTEC for supplying the intermetallic material. During the preparation of this manuscript/study, the authors used ChatGPT (GPT-5.2, OpenAI, 2026) for the purposes of English language editing and stylistic refinement. The authors have reviewed and edited the output and take full responsibility for the content of this publication. This article is dedicated to the memory of our colleague Frédéric Thiébaud, who passed away during its writing. The authors are deeply grateful to him for his lasting contributions, insightful scientific discussions, and valuable reflections.

Conflicts of Interest: Author Aurélien Neveu was employed by the company Granutools. The remaining authors declare that the research was conducted in the absence of any commercial or financial relationships that could be construed as a potential conflict of interest.

References

1. Ajanovic, A.; Sayer, M.; Haas, R. On the Future Relevance of Green Hydrogen in Europe. *Appl. Energy* **2024**, *358*, 122586. https://doi.org/10.1016/j.apenergy.2023.122586.
2. Nnabuife, S.G.; Yang, J.; Kuang, B.; Akpala-Okoroafor, E.N.; Onwualu, P.A. Optimising Hydrogen Carrier Pathways for Industrial Decarbonisation: A Techno-Policy Framework for Readiness in Infrastructure and Governance. *Int. J. Hydrogen Energy* **2025**, *178*, 151612. https://doi.org/10.1016/j.ijhydene.2025.151612.
3. Reda, B.; Elzamar, A.A.; AlFazzani, S.; Ezzat, S.M. Green Hydrogen as a Source of Renewable Energy: A Step towards Sustainability, an Overview. *Environ. Dev Sustain* **2025**, *27*, 29213–29233. https://doi.org/10.1007/s10668-024-04892-z.
4. Magliano, A.; Perez Carrera, C.; Pappalardo, C.M.; Guida, D.; Berardi, V.P. A Comprehensive Literature Review on Hydrogen Tanks: Storage, Safety, and Structural Integrity. *Appl. Sci.* **2024**, *14*, 9348. https://doi.org/10.3390/app14209348.
5. Aziz, M. Liquid Hydrogen: A Review on Liquefaction, Storage, Transportation, and Safety. *Energies* **2021**, *14*, 5917. https://doi.org/10.3390/en14185917.
6. Hassan, N.S.; Jalil, A.A.; Izzuddin, N.M.; Alatawi, A.A.; Alhassan, M.; Muttaqii, M.A.; Rajendran, S.; Bahari, M.B. Research Progress and Techno-Economic Assessment of Cryo-Compressed Hydrogen Storage for Clean and Sustainable Energy. *Int. J. Hydrogen Energy* **2026**, *220*, 154107. https://doi.org/10.1016/j.ijhydene.2026.154107.
7. Wijayanta, A.T.; Oda, T.; Purnomo, C.W.; Kashiwagi, T.; Aziz, M. Liquid Hydrogen, Methylcyclohexane, and Ammonia as Potential Hydrogen Storage: Comparison Review. *Int. J. Hydrogen Energy* **2019**, *44*, 15026–15044. https://doi.org/10.1016/j.ijhydene.2019.04.112.
8. Hirscher, M.; Yartys, V.A.; Baricco, M.; Bellosta von Colbe, J.; Blanchard, D.; Bowman, R.C.; Broom, D.P.; Buckley, C.E.; Chang, F.; Chen, P.; et al. Materials for Hydrogen-Based Energy Storage—Past, Recent Progress and Future Outlook. *J. Alloys Compd.* **2020**, *827*, 153548. https://doi.org/10.1016/j.jallcom.2019.153548.
9. Alharthi, L.; Hazazi, K.; Alanazi, A.; Bokhari, A. Hydrogen Storage in Carbon Materials: A Review of Mechanisms, Performance, and Optimization Strategies. *Renew. Sustain. Energy Rev.* **2026**, *231*, 116751. https://doi.org/10.1016/j.rser.2026.116751.
10. Xi, S.; Gao, L.; Yao, W.; Huang, J.; Chen, R.; Wu, W.; Xu, D.; Dong, X.; Wang, H.; Gong, M.; et al. Study on the Low-Temperature and High-Pressure Hydrogen Storage Performance of MIL-101(Cr)-Filled Type III Tank. *Int. J. Hydrogen Energy* **2025**, *128*, 95–104. https://doi.org/10.1016/j.ijhydene.2025.04.219.
11. Scarpati, G.; Frasci, E.; Di Ilio, G.; Jannelli, E. A Comprehensive Review on Metal Hydrides-Based Hydrogen Storage Systems for Mobile Applications. *J. Energy Storage* **2024**, *102*, 113934. https://doi.org/10.1016/j.est.2024.113934.
12. Liu, Y.; Chabane, D.; Elkedim, O. Intermetallic Compounds Synthesized by Mechanical Alloying for Solid-State Hydrogen Storage: A Review. *Energies* **2021**, *14*, 5758. https://doi.org/10.3390/en14185758.
13. Liu, W.; Tupe, J.A.; Aguey-Zinsou, K.-F. Metal Hydride Storage Systems: Approaches to Improve Their Performances. *Part. Part. Syst. Charact.* **2025**, *42*, 2400163. https://doi.org/10.1002/ppsc.202400163.
14. Sdanghi, G.; Maranzana, G.; Celzard, A.; Fierro, V. Review of the Current Technologies and Performances of Hydrogen Compression for Stationary and Automotive Applications. *Renew. Sustain. Energy Rev.* **2019**, *102*, 150–170. https://doi.org/10.1016/j.rser.2018.11.028.
15. Marques, F.; Balcerzak, M.; Winkelmann, F.; Zepon, G.; Felderhoff, M. Review and Outlook on High-Entropy Alloys for Hydrogen Storage. *Energy Environ. Sci.* **2021**, *14*, 5191–5227. https://doi.org/10.1039/D1EE01543E.
16. Somo, T.R.; Lototskyy, M.V.; Yartys, V.A.; Davids, M.W.; Nyamsi, S.N. Hydrogen Storage Behaviours of High Entropy Alloys: A Review. *J. Energy Storage* **2023**, *73*, 108969. https://doi.org/10.1016/j.est.2023.108969.
17. Agafonov, A.; Pineda-Romero, N.; Witman, M.; Nassif, V.; Vaughan, G.B.M.; Lei, L.; Ling, S.; Grant, D.M.; Dornheim, M.; Allendorf, M.; et al. Destabilizing High-Capacity High Entropy Hydrides via Earth Abundant Substitutions: From Predictions to Experimental Validation. *Acta Mater.* **2024**, *276*, 120086. https://doi.org/10.1016/j.actamat.2024.120086.
18. Cuevas, F.; Latroche, M. Des Matériaux Qui Stockent de l'hydrogène sans Effort. *Bull. L'union Profr. Phys. Chim.* **2022**, *116*, 69–74.
19. Reid, C.; Liu, W.; Aguey-Zinsou, K. Metal Hydrides-Based Hydrogen Purification Systems—A Review. *MetalMat* **2025**, *3*, e70025. https://doi.org/10.1002/metm.70025.
20. Peng, Z.; Li, Q.; Ouyang, L.; Jiang, W.; Chen, K.; Wang, H.; Liu, J.; Li, Z.; Wang, S.; Zhu, M. Overview of Hydrogen Compression Materials Based on a Three-Stage Metal Hydride Hydrogen Compressor. *J. Alloys Compd.* **2022**, *895*, 162465. https://doi.org/10.1016/j.jallcom.2021.162465.
21. Qin, F. Pulverization, Expansion of $La_{0.6}Y_{0.4}Ni_{4.8}Mn_{0.2}$ during Hydrogen Absorption–Desorption Cycles and Their Influences in Thin-Wall Reactors. *Int. J. Hydrogen Energy* **2008**, *33*, 709–717. https://doi.org/10.1016/j.ijhydene.2007.10.029.

22. Okumura, M.; Ikado, A.; Saito, Y.; Aoki, H.; Miura, T.; Kawakami, Y. Pulverization Mechanism of Hydrogen Storage Alloys on Microscale Packing Structure. *Int. J. Hydrogen Energy* **2012**, *37*, 10715–10723. https://doi.org/10.1016/j.ijhydene.2012.04.061.
23. Charlas, B.; Gillia, O.; Doremus, P.; Imbault, D. Experimental Investigation of the Swelling/Shrinkage of a Hydride Bed in a Cell during Hydrogen Absorption/Desorption Cycles. *Int. J. Hydrogen Energy* **2012**, *37*, 16031–16041. https://doi.org/10.1016/j.ijhydene.2012.07.091.
24. Okumura, M.; Terui, K.; Ikado, A.; Saito, Y.; Shoji, M.; Matsushita, Y.; Aoki, H.; Miura, T.; Kawakami, Y. Investigation of Wall Stress Development and Packing Ratio Distribution in the Metal Hydride Reactor. *Int. J. Hydrogen Energy* **2012**, *37*, 6686–6693. https://doi.org/10.1016/j.ijhydene.2012.01.097.
25. Okumura, M.; Ikado, A.; Saito, Y.; Matsushita, Y.; Aoki, H.; Kawakami, Y. The stress developed on the side wall of the pressure vessel for the packed bed of the hydrogen storage alloy and the change in the packing state. *J. Jpn. Inst. Energy* **2021**, *100*, 5–12. https://doi.org/10.3775/jie.100.5.
26. Ao, B.Y.; Chen, S.X.; Jiang, G.Q. A Study on Wall Stresses Induced by $LaNi_5$ Alloy Hydrogen Absorption–Desorption Cycles. *J. Alloys Compd.* **2005**, *390*, 122–126. https://doi.org/10.1016/j.jallcom.2004.05.092.
27. Stahlkopf, G.; Passing, M.; Puszkiel, J.A.; Moosmann, J.; Beckmann, F.; Warfsmann, J.; Karimi, F.; Kulvait, V.; Klassen, T.; Jepsen, J. Insights on Mechanical and Morphological Metal Hydride Powder Characteristics during Hydrogen Interaction and Stress Mitigation Strategies for Hydrogen Storage Vessels. *Int. J. Hydrogen Energy* **2026**, *215*, 153776. https://doi.org/10.1016/j.ijhydene.2026.153776.
28. Granutools GranuHeap: Granular Material Heap Analyzer. Available online: https://www.granutools.com/en/granuheap (accessed on 20 October 2025).
29. Bebon, L.; Maynadier, A.; Gaillard, Y.; Chapelle, D. Multiscale Elastic Modulus Characterization of $Ti_{0.5}Fe_{0.45}Mn_{0.05}$, an Iron–Titanium–Manganese Alloy Dedicated to Hydrogen Storage. *Materials* **2024**, *17*, 6100. https://doi.org/10.3390/ma17246100.
30. Sandrock, G. A Panoramic Overview of Hydrogen Storage Alloys from a Gas Reaction Point of View. *J. Alloys Compd.* **1999**, *293*, 877–888. https://doi.org/10.1016/S0925-8388(99)00384-9.
31. Dematteis, E.M.; Dreistadt, D.M.; Capurso, G.; Jepsen, J.; Cuevas, F.; Latroche, M. Fundamental Hydrogen Storage Properties of TiFe-Alloy with Partial Substitution of Fe by Ti and Mn. *J. Alloys Compd.* **2021**, *874*, 159925. https://doi.org/10.1016/j.jallcom.2021.159925.
32. Reilly, J.J.; Wiswall, R.H. Formation and Properties of Iron Titanium Hydride. *Inorg. Chem.* **1974**, *13*, 218–222.
33. Lin, C.-K.; Chen, Y.-C. Effects of Cyclic Hydriding–Dehydriding Reactions of LaNi5 on the Thin-Wall Deformation of Metal Hydride Storage Vessels with Various Configurations. *Renew. Energy* **2012**, *48*, 404–410. https://doi.org/10.1016/j.renene.2012.05.024.
34. Neveu, A.; Francqui, F.; Lumay, G. Measuring Powder Flow Properties in a Rotating Drum. *Measurement* **2022**, *200*, 111548. https://doi.org/10.1016/j.measurement.2022.111548.
35. Fiscina, J.E.; Lumay, G.; Ludewig, F.; Vandewalle, N. Compaction Dynamics of Wet Granular Assemblies. *Phys. Rev. Lett.* **2010**, *105*, 048001. https://doi.org/10.1103/PhysRevLett.105.048001.
36. Hausner, H.H. Friction Conditions in a Mass of Metal Powder. *Int. J. Powder Met.* **1967**, *3*, 7–13.
37. Carr, R.L. Evaluating Flow Properties of Solids. *Chem. Eng.* **1965**, *72*, 163–168.
38. Kadiri, M.S. Compression de Poudres Pharmaceutiques et Interaction Avec L'outillage. Ph.D. Thesis, Institut National Polytechnique, Toulouse, France, 2004.
39. A, J.H. Versuche Uber Getreidedruck in Silozellen. *VDI Z.* **1895**, *39*, 1045–1049.
40. Strutt, J.W. *Scientific Papers: Volume 5: 1902–1910*; Cambridge Library Collection—Mathematics; Cambridge University Press: Cambridge, UK, 2009; Volume 5.
41. Visser, J. Van Der Waals and Other Cohesive Forces Affecting Powder Fluidization. *Powder Technol.* **1989**, *58*, 1–10. https://doi.org/10.1016/0032-5910(89)80001-4.
42. Parrish, J.R. Packing of Spheres. *Nature* **1961**, *190*, 800. https://doi.org/10.1038/190800a0.
43. Li, Y.; Buscarnera, G. Role of the Particle Size and Shape Dispersion on Stress Transmission and Strain Energy Storage. *Geotech. Lett.* **2025**, *15*, 45–51. https://doi.org/10.1680/jgele.24.00056.
44. Gillia, O. Hydride Breathing and Its Consequence on Stresses Applied to Containers: A Review. *Int. J. Hydrogen Energy* **2021**, *46*, 35594–35640. https://doi.org/10.1016/j.ijhydene.2021.07.082.
45. Lanzerstorfer, C.; Forsich, C.; Delfin, F.; Schachinger, M.C.J.; Heim, D. Reduction in Powder Wall Friction by an A-C:H:Si Film. *Materials* **2024**, *17*, 2421. https://doi.org/10.3390/ma17102421.

46. Matsushita, M.; Monde, M.; Mitsutake, Y. Experimental Formula for Estimating Porosity in a Metal Hydride Packed Bed. *Int. J. Hydrogen Energy* **2013**, *38*, 7056–7064. https://doi.org/10.1016/j.ijhydene.2013.04.005.
47. Nasako, K.; Ito, Y.; Hiro, N.; Osumi, M. Stress on a Reaction Vessel by the Swelling of a Hydrogen Absorbing Alloy. *J. Alloys Compd.* **1998**, *264*, 271–276. https://doi.org/10.1016/S0925-8388(97)00246-6.
48. Lin, C.-K.; Huang, S.-M.; Jhang, Y.-H. Effects of Cyclic Hydriding–Dehydriding Reactions of Mg_2Ni Alloy on the Expansion Deformation of a Metal Hydride Storage Vessel. *J. Alloys Compd.* **2011**, *509*, 7162–7167. https://doi.org/10.1016/j.jallcom.2011.04.038.